Modeling and Control of a Superimposed Steering System

A Thesis
Presented to
The Academic Faculty

by

Bjoern Avak

In Partial Fulfillment
of the Requirements for the Degree
Master of Science

School of Electrical and Computer Engineering
Georgia Institute of Technology
July 2004

Modeling and Control of a Superimposed Steering System

Approved by:

Dr. David G. Taylor, Advisor

Dr. Magnus Egerstedt

Dr. Bonnie S. Heck-Ferri

July 9, 2004

ACKNOWLEDGEMENTS

I would like to thank my advisor, Dr. David G. Taylor, for his support and for giving me such a great amount of freedom in determining the thesis topic. His guidance has been invaluable. I would also like to thank Dr. Magnus Egerstedt and Dr. Bonnie S. Heck-Ferri for being part of my thesis committee.

I gratefully acknowledge the assistance of Dr. Farrokh Mistree in making things happen. His ideas have been a source of inspiration throughout my graduate studies and will continue to be so.

Finally, I thank my family for their love and support through all these years.

TABLE OF CONTENTS

LIST OF TABLES

LIST OF FIGURES

CHAPTER I

INTRODUCTION

1.1 Motivation for Superimposed Steering

The research focus both in the industry and in academia has been on steer-by-wire systems for a long time. In such systems one removes the direct mechanical linkage between the steering wheel and the actual wheels. The envisaged benefits are reduced weight and complexity, as well as better power management and vehicle stability improvement. Further research has however indicated that a complete steer-by-wire system is economically infeasible, at least in the near future [6]. Due to legal and safety concerns, all major components of the steer-by-wire system would have to be installed redundantly making the cost prohibitive compared to conventional steering systems. Moreover, in a conventional steering system the driver gets important information about road friction and vehicle stability through the direct mechanical linkage of the steering wheel with the wheels. Since this linkage does not exist in a steer-by-wire system, one would have to introduce synthetic feedback. Hence, although steer-by-wire is technically possible today, it will not be actually implemented in vehicles for several years to come.

That is why the emerging trend in the automotive industry is to introduce hybrid systems such as superimposed steering systems. In these systems one maintains the mechanical linkage between the steering wheel and the wheels, but installs an electric motor in the steering column. The electric motor is used to increase or decrease the road-wheel angle imposed by the driver as a function of vehicle velocity, vehicle stability, and the driver's steering wheel angle. Most of the advantages of a steer-by-wire system can be obtained using a superimposed system without the above technical and legal problems. The major advantages of a superimposed steering system over a conventional steering system can be broken down into three main categories.

1.1.1 Variable Steering Ratio

The steering ratio is defined as the quotient of the angle that the driver imposes on the steering wheel over the actual angle of the wheels on the road. In a conventional steering system this ratio is fixed (typically 17). However, this is not the best possible solution. At low speeds one would rather want a more direct response of the wheels to the driver's commands, i.e., a lower steering ratio. The vehicle would thus become more agile and parking could be greatly facilitated. At high speeds, one would want the steering transmission to be less direct, i.e., higher steering ratio. This would result in greater vehicle stability due to the compensation for the physically induced increase in steering sensitivity. All this can be achieved using a superimposed steering system (Figure 1). A variable steering ratio is implemented by adding a positive steering angle at low speed and a negative steering angle at high speed. In this thesis we focus on bringing about this first and most important

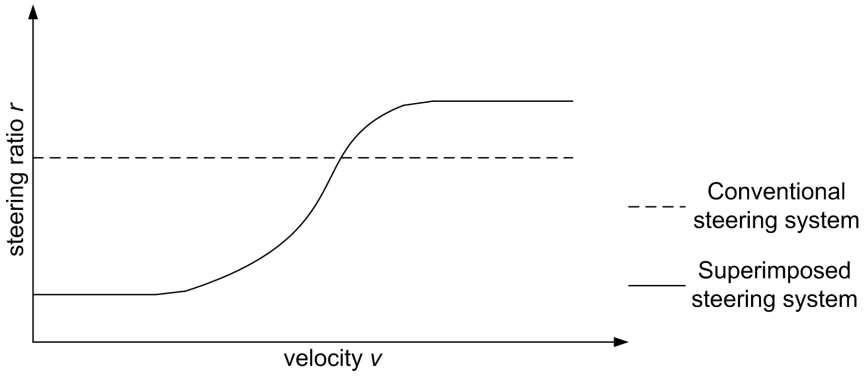

Figure 1: Steering ratio.

advantage of a superimposed steering system.

1.1.2 Compensation of Lateral Wind Forces

Lateral wind forces affect the vehicle handling and represent a major risk, especially when passing other vehicles at high velocity. Using superimposed steering, one can automatically compensate for lateral wind forces. A yaw rate sensor detects the lateral acceleration and the superimposed steering system compensates without the driver even noticing.

1.1.3 Reduction of Braking Distance in Combination with ESP

Traditional electronic stability programs (ESP) maintain the stability of the vehicle through multiple braking and release cycles of the wheels. The result is a tradeoff between stability and braking distance. This is particularly critical if the vehicle drives on two surfaces with highly different friction coefficients, e.g., asphalt and ice. The vehicle will invariably turn towards one side. Stability can only be regained by releasing the brakes thus increasing braking distance. Combining ESP with superimposed steering, the vehicle will automatically steer so as to compensate for the turning of the vehicle. As a result more power can be applied to the brakes and braking distance can be reduced.

1.2 Structure of this Thesis

The structure of this thesis breaks down into eight chapters (Figure 2). In Chapter 1 we

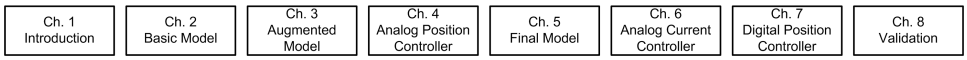

Figure 2: Overview of thesis.

introduce and motivate the concept of a superimposed steering system for more comfortable and safer driving. In Chapters 2 and 3 we set up the first model of the system. We start with the basic model comprising the vehicle dynamics and the tire-road interface. The basic model is then augmented with a simple model of the steering system. This approach is facilitated by the use of modularity. In Chapter 4 we introduce the first controller. It is analog and derived under the assumption that the motor is an ideal torque source. The system model is improved in Chapter 5 by incorporating the internal dynamics of the electric motor. In Chapter 6 we also take the controller to this level of detail by designing an analog current controller. In Chapter 7 we motivate and implement direct digital design of the torque controller. We thus move the analog controller from Chapter 4 to the digital domain. Finally, we validate our design using the Validation Square technique in Chapter 8.

1.3 Nomenclature

In the following we give the symbols used in this thesis and their respective units. We use SI units. The focus is on symbols that appear in the actual model or controller, i.e., symbols merely used during derivation are not included.

Global parameters		
α_f	front slip angle	[rad]
α_r	rear slip angle	[rad]
β	vehicle sideslip angle	[rad]
δ_f	road-wheel angle	[rad]
F_f	front cornering force	[N]
F_r	rear cornering force	[N]
F_W	lateral wind force	[N]
γ	vehicle yaw rate	[rad/sec]
v	vehicle velocity	[m/sec]

Table 1: Global parameters.

Vehicle module		
J_V	vehicle mass moment of inertia	[kgm^2]
l_f	distance CG to front axle	[m]
l_r	distance CG to rear axle	[m]
m	vehicle mass	[kg]
Friction module		
c_f	front cornering stiffness	[kN/rad]
c_r	rear cornering stiffness	[kN/rad]

Table 2: Vehicle and friction modules.

Steering module		
C_M	Coulomb constant of PMSM	[Nm]
C_S	Coulomb constant of steering system	[Nm]
δ_{SW}	steering wheel angle	[rad]
δ_{sup}	superimposed steering angle	[rad]
$\delta_{sup_{des}}$	desired superimposed steering angle	[rad]
G_S	gear ratio of steering system	
G_H	gear ratio of harmonic drive	
i_a, i_b, i_c	phase currents	[A]
i_q, i_d	quadrature-/direct-axis current	[A]
J_{Load}	total mass moment of inertia of load	[kgm^2]
J_M	mass moment of inertia of PMSM rotor	[kgm^2]
J_S	mass moment of inertia of steering column	[kgm^2]
J_W	mass moment of inertia of front wheels	[kgm^2]
L	PMSM self inductance	[H]
L'	PMSM inductance	[H]
λ_m	flux magnitude	[Wb]
M	PMSM mutual inductance	[H]
m_r	mass of steering rack	[kg]
N	PMSM number of pole pairs	
R	PMSM resistance	[Ω]
r_p	radius of pinion	[m]
T_L	load torque	[Nm]
T_M	motor torque	[Nm]
v_a, v_b, v_c	phase voltages	[V]
v_q, v_d	quadrature-/direct-axis voltage	[V]

Table 3: Steering module.

Controller		
K_1, K_2	state feedback gains of torque controller	
K_I	current integral gain	
K_{IS}	integral state gain of torque controller	
K_P	current proportional gain	
L_r	estimator feedback gain	
ω_0	natural frequency of torque controller	[sec^{-1}]
ω_1	natural frequency of current controller	[sec^{-1}]
T	sampling period	[sec]
T_D	disturbance torque	[Nm]
T_{fb}	digital torque controller feedback torque	[Nm]
T_{ff}	digital torque controller feedforward torque	[Nm]

Table 4: Controller.

CHAPTER II

BASIC MODEL - VEHICLE AND FRICTION MODULES

In this chapter we present the structure of the modular simulation model comprising three main modules. We also describe the two modules that will remain unchanged throughout this work, i.e. the steering and friction modules. The simulation model will be augmented and improved in Chapters 3 and 5.

2.1 Modular Modeling Approach

We have divided the entire simulation model for the superimposed steering system into several modules (Figure 3). There are two reasons for this. First, a modular system is easier to understand, because it reflects the physical structure of the system. Modules can also be considered individually. Second, a modular approach provides greater flexibility. The model can be adapted to specific needs just by modifying individual modules. These changes can be implemented easily, because there is no need to redesign the model as a whole. There are two inputs to the simulation model, namely the vehicle velocity v and the

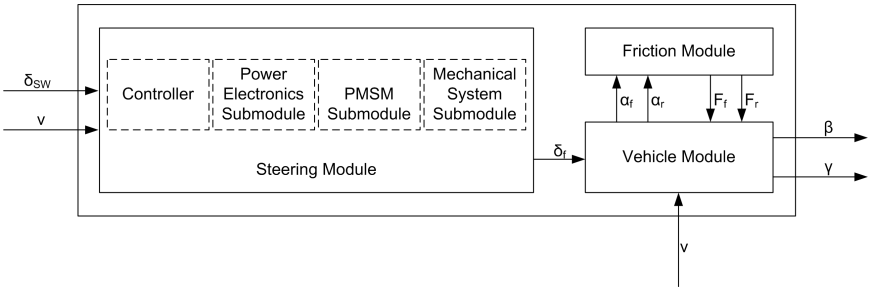

Figure 3: Modular simulation model.

steering wheel angle δ_{SW}. δ_{SW} and v are both controlled by the driver.

Within the simulation model, there are three main modules, the steering module, the vehicle module, and the friction module. The steering module comprises the controller, the

power electronics submodule, the permanent-magnet synchronous motor (PMSM) submodule, and the mechanical steering system submodule. The modules interact through several global parameters. In the steering module the road-wheel angle δ_f is calculated based on the velocity v and the steering wheel angle δ_{SW}. The road-wheel angle δ_f is input to the vehicle module where the vehicle yaw rate γ and the sideslip angle β are calculated. In order to do so, one needs the front and rear cornering forces F_f and F_r. F_f and F_r are the outputs of the friction module, which requires the front and rear slip angles α_f and α_r as inputs.

There are also several internal parameters within each module. These will be introduced with the individual modules.

2.2 Vehicle Module

The model used for the vehicle module is based on the bicycle or single-track model as first developed in [20]. In this model both the two front wheels and the two rear wheels are lumped into one wheel at the center line of the vehicle (Figure 4). The body coordinate

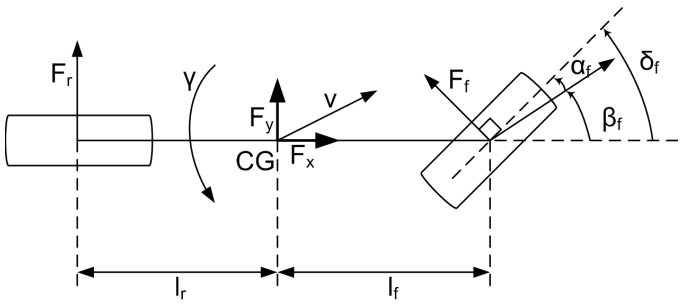

Figure 4: Single-track vehicle model.

system is defined by the longitudinal x-axis and the lateral y-axis of the vehicle.

In addition to the global parameters outlined above the following parameters are needed for the vehicle module. The distance from the front axle to the center of gravity (CG) is l_f. Similarly l_r is the distance from CG to the rear axle. The vehicle has the mass m and the mass moment of inertia J_V.

The following parameters have already been introduced above, but will be explained in

more detail here. The sideslip angle β is defined as the angle between the direction of the vehicle velocity and the center line of the vehicle. The road-wheel angle δ_f is the angle between the direction of the velocity of the front wheel and the center line of the vehicle. The front slip angle α_f is defined as the angle between the center line of the front wheel and the direction of the velocity of the front wheel. Similarly α_r is the angle between the center line of the rear wheel and the direction of the velocity of the rear wheel.

It is assumed that the vehicle operates on a flat plane. The only external forces affecting the vehicle are the cornering forces F_f and F_r. The cornering forces occur at the contact surface between the wheels and the road. These forces are calculated as part of the friction module.

2.2.1 First Equation of Single-Track Model

The front and rear cornering forces can be separated into x- and y-components, i.e.,

$$\begin{aligned} F_x &= -\sin\delta_f F_f \\ F_y &= \cos\delta_f F_f + F_r \end{aligned} \tag{1}$$

or

$$\begin{bmatrix} F_x \\ F_y \end{bmatrix} = \begin{bmatrix} -\sin\delta_f & 0 \\ \cos\delta_f & 1 \end{bmatrix} \begin{bmatrix} F_f \\ F_r \end{bmatrix} \tag{2}$$

The differential equations can be derived from Newton's second law, which says that the acceleration times the mass is equal to the sum of all forces. In mathematical terms this is

$$ma = \sum_i F_i \tag{3}$$

If we apply Newton's law to the different forces acting in the lateral direction with respect to the vehicle's velocity, we obtain

$$ma_y = -\sin\beta F_x + \cos\beta F_y = \begin{bmatrix} -\sin\beta & \cos\beta \end{bmatrix} \begin{bmatrix} F_x \\ F_y \end{bmatrix} \tag{4}$$

The expression for a_y is derived using vector analysis. The acceleration of a rotating and translating body in space is given by the expression

$$\mathbf{a} = \gamma \times \mathbf{v} + \dot{\mathbf{v}} \tag{5}$$

which can be found in [21]. By calculating the vector product one gets

$$\mathbf{a} = \gamma \mathbf{e_z} \times v\mathbf{e_x} + \dot{\mathbf{v}} = \gamma v \mathbf{e_y} + \dot{v}\mathbf{e_y} = v(\gamma + \dot{\beta})\mathbf{e_y} \tag{6}$$

The results of (2), (4) and (6) are taken together resulting in

$$\begin{aligned} mv(\dot{\beta} + \gamma) &= \begin{bmatrix} -\sin\beta & \cos\beta \end{bmatrix} \begin{bmatrix} -\sin\delta_f & 0 \\ \cos\delta_f & 1 \end{bmatrix} \begin{bmatrix} F_f \\ F_r \end{bmatrix} \\ mv(\dot{\beta} + \gamma) &= \begin{bmatrix} \sin\beta\sin\delta_f + \cos\beta\cos\delta_f & \cos\beta \end{bmatrix} \begin{bmatrix} F_f \\ F_r \end{bmatrix} \end{aligned} \tag{7}$$

2.2.2 Second Equation of Single-Track Model

The second differential equation is based on the fact that the sum of all torques must be equal to the mass moment of inertia J times the angular acceleration $\ddot{\alpha}$, i.e.,

$$\sum_i M_i = J\ddot{\alpha} \tag{8}$$

Torque is the product between the torque arm and the component of the force that is orthogonal to it and therefore

$$M = rF \tag{9}$$

As already noted in the derivation of the first equation, the external forces affecting the vehicle are the cornering forces F_f and F_r on the front and rear wheels. Considering the distance between the point of application of the forces and the center of gravity as well as the angles between the vectors, one obtains

$$J_V\dot{\gamma} = F_f l_f \cos\delta_f - F_r l_r \tag{10}$$

Equations (7) and (10) can be summarized in the single vector-matrix equation

$$\begin{bmatrix} mv(\dot{\beta} + \gamma) \\ J_V\dot{\gamma} \end{bmatrix} = \begin{bmatrix} \sin\beta\sin\delta_f + \cos\beta\cos\delta_f & \cos\beta \\ l_f\cos\delta_f & -l_r \end{bmatrix} \begin{bmatrix} F_f \\ F_r \end{bmatrix} \tag{11}$$

2.2.3 Slip Angles

The slip angles were already mentioned in the introduction to the modular simulation model. The actual calculation is given here. The rear slip angle is defined as the rear wheel lateral velocity divided by the forward velocity. Hence, the rear slip angle is a function of the vehicle velocity v, the yaw rate γ, and the sideslip angle β. The two latter parameters are the state variables of the single-track model. The rear slip angle is

$$\alpha_r = \frac{-\beta v + l_r \gamma}{v} = -\beta + \frac{l_r}{v}\gamma \tag{12}$$

Similarly the front slip angle is defined as the front wheel lateral velocity divided by the forward velocity minus the steering angle. It is therefore

$$\alpha_f = \frac{-\beta v + l_f \gamma}{v} - \delta_f = -\delta_f - \beta + \frac{l_f}{v}\gamma \tag{13}$$

2.3 Friction Module

Many types of friction models can be found in the literature. The most simple approach is a linear model such as it has been used in [14] and [18]. Some authors ([8], [17], [22]) use a static nonlinear model commonly referred to as the magic formula or Pacejka model ([1]). The most complex friction models used are dynamic models such as the one developed in [5].

We use a linear tire model and assume the cornering forces to be a linear function of the slip angles α_f, α_r. Cornering forces and slip angles are thus related by means of the cornering stiffnesses c_f, c_r, which are proportionality constants. With this the cornering forces can be calculated from

$$\begin{aligned} F_f &= c_f \alpha_f \\ F_r &= c_r \alpha_r \end{aligned} \tag{14}$$

In order to calculate the cornering forces, one therefore only needs the front and rear slip angles α_f and α_r from the vehicle module. The resulting cornering forces F_f and F_r are returned to the vehicle model (Figure 5).

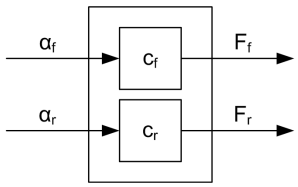

Figure 5: Friction module.

2.4 Parameters of Vehicle and Friction Modules

We have chosen to design the superimposed steering model and controller for a small truck. The vehicle parameters have been chosen to reflect this.

2.4.1 Parameters of Vehicle Module

The parameters of the truck have been based on the assumption that the vehicle is laden to its maximum permissible weight. This is the worst case scenario from the point of view of driving dynamics. Hence, the weight of the truck is $m = 2940$ kg. The wheelbase is 3200 mm. The distance of the center of gravity (CG) to the rear axle is $l_r = 1513$ mm. As a result the distance from CG to the front axle is $l_f = 1687$ mm. The vehicle mass moment of inertia is $J_V = 4300$ kgm^2.

2.4.2 Parameters of Friction Module

The tire forces for the type of tire to be used for the truck have been measured at the Technical University of Dresden in February 1998. The tire has been analyzed on a tire test bench at a speed of 11.1 m/s. The internal pressure of the tire was 2.9 bar.

We will first obtain the cornering stiffness of one individual tire and then calculate the stiffness for the single-track vehicle model by multiplying the results by two. The weight on each of the two front wheels is $\frac{m}{2}\frac{l_r}{l_f+l_r} = 695$ kg and on the two rear wheels $\frac{m}{2}\frac{l_f}{l_f+l_r} = 775$ kg. The resulting wheel loads are 6.818 kN for the front wheels and 7.603 kN for the rear wheels. The measurements for the cornering forces $F_{f/r}$ as a function of the front/rear slip angle $\alpha_{f/r}$ have been executed for a wheel load of 6.0 kN and 9.0 kN. The results can be found in Figure 6. As one can see from the figure, the behavior of the cornering forces $F_{f/r}$ is approximately linear for $\alpha_{f/r} \in [-0.05, 0.05]$. That is why we can use the friction model

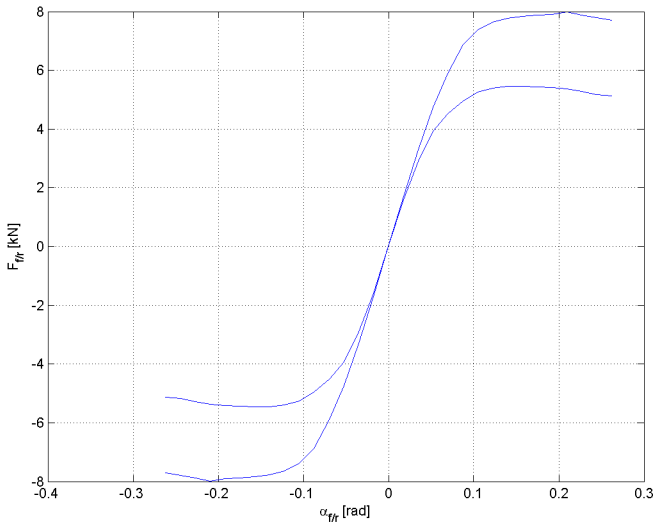

Figure 6: Measurements of cornering forces.

as described in Section 2.3. We define the cornering stiffness as the slope of the curve at the origin. In this instance the cornering stiffness is 90.457 kNrad^{-1} for each of the front tires and 97.886 kNrad^{-1} for each of the rear tires. Since we use the single-track model, we have to lump the tires at the front and at the back. Hence, the front cornering stiffness is $c_f = 180.914$ kNrad^{-1} and the rear cornering stiffness is $c_r = 195.772$ kNrad^{-1}.

The vehicle and friction parameters of the truck are summarized in Table 5.

Vehicle module		
l_f	distance CG to front axle	1687 mm
l_r	distance CG to rear axle	1513 mm
m	vehicle mass	2940 kg
J_V	vehicle mass moment of inertia	4300 kgm^2
Friction module		
c_f	front cornering stiffness	180.914 kNrad^{-1}
c_r	rear cornering stiffness	195.772 kNrad^{-1}

Table 5: Vehicle and friction parameters of small truck.

CHAPTER III

AUGMENTED MODEL - LOW-DETAIL STEERING MODULE

In this chapter we present the low-detail steering module. Together with the vehicle and friction modules presented in Chapter 2 this gives us the complete augmented simulation model of the system. The low-detail steering module presented here differs from the high-detail steering module presented in Chapter 5 in that the electric motor is assumed to be an ideal torque source whereas in Chapter 5 we model the internal dynamics of the motor.

3.1 Structure of Low-Detail Steering Module

There are many approaches to modeling the steering system. These differ greatly in accuracy and level of complexity. In most publications focusing on control, very simple steering models are employed. The authors assume the additional steering angle to be a direct output of the controller ([5], [17], [18]). A more realistic approach is used in [8] where the entire steering system is modeled as a first-order system. The most sophisticated approach can be found in [15]. In this paper the driver input has been modeled as a torque. The electric motor for the superimposed steering system adds an additional torque. The system is damped by the mass moment of inertia of the wheels and the steering system itself. The wheel torque due to the caster angle offset has been modeled as well.

The model that is used here is a modified version of the model in [15]. The entire steering system is broken down into the subsystems of the controller, the power electronics, the permanent-magnet synchronous motor (PMSM), and the mechanical system (Figure 7).

The inputs to the steering module are the steering wheel angle δ_{SW} and the vehicle velocity v. Based on these inputs and the superimposed steering angle δ_{sup}, a desired vector of voltages $\underline{v}_{des}$ is calculated in the controller. These voltages are amplified in the

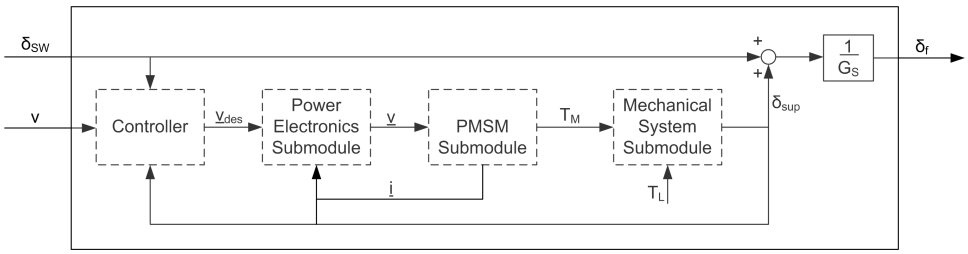

Figure 7: Steering module.

power electronics and supplied to the permanent-magnet synchronous motor. The output of the motor is the motor torque T_M. In the mechanical system submodule the resulting superimposed steering angle δ_{sup} is calculated from T_M and the load torque T_L. δ_{sup} is added to δ_{SW} and divided by the gear ratio of the steering system G_S to obtain the road-wheel angle δ_f which is the output of the steering module.

In the low-detail steering model described in this chapter we simplify the steering module by assuming that the motor torque T_M is a direct output of the controller. This can be seen in Figure 8. That is why we only deal with the mechanical system submodule in this chapter. The power electronics and PMSM submodules are dealt with in Chapter 5.

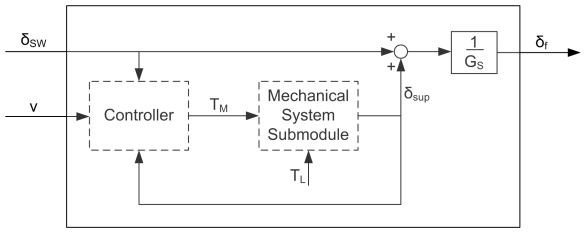

Figure 8: Low-detail steering module.

3.2 Mechanical System Submodule

We first derive the equations of the mechanical system and then show how to calculate the inertia of the load.

3.2.1 Equations of Mechanical System

In the mechanical system submodule we describe the mechanical dynamics of the steering system. A schematic of the envisaged mechanical system can be seen in Figure 9.

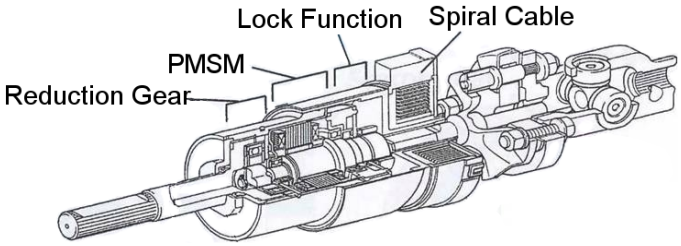

Figure 9: Schematic of superimposed steering system.

The load torque for the electric motor depends primarily on the location of the motor in the steering system. If the superimposed steering system is located below the power steering system, then the required torque is a function of the steering system and the road conditions. The primary driver in this case is the self-alignment torque. If the superimposed steering system is located above the power steering system, then the required torque also depends on the power steering system. The latter approach is chosen for the implementation of the superimposed steering system in the truck, because this is the only way to keep the PMSM small and light. If the superimposed steering system were not supported by the power steering system, one would need a large and heavy PMSM.

Apart from the load torque the system is also slowed down by friction both in the steering system and in the PMSM itself. We have modeled this using Coulomb friction. The Coulomb constant of the motor is C_M and the Coulomb constant of the steering system is C_S.

Continuing on our intention of keeping the PMSM small and light we use a harmonic drive with a gear ratio of G_H. A harmonic drive is a gear set that is very precise and has extremely low friction. This is achieved by having two gears with a slightly different number of teeth, e.g., 100 and 102. The harmonic drive used here has a gear ratio of G_H (Figure 10). By abstracting from Figure 10 to a more generic representation of a gear coupled system we obtain Figure 11. The motor rotates at a G_H times higher speed than the load. As a result of the gear set, the effect of the load torque T_L and the load inertia J_{Load} can be reduced. We use this abstracted representation. The Euler equation for the gear coupled system in

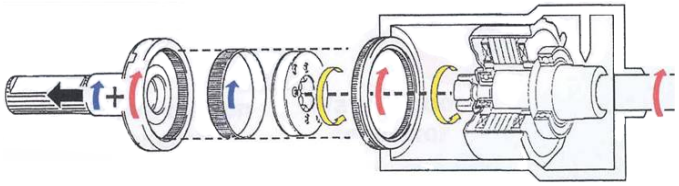

Figure 10: Harmonic drive.

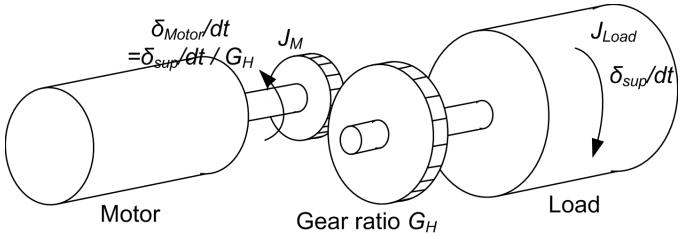

Figure 11: Gear coupled system.

the frame of reference of the motor is

$$J_M \frac{\mathrm{d}^2\delta_{Motor}}{\mathrm{d}t^2} + J_{Load}\frac{\mathrm{d}^2\delta_{sup}}{\mathrm{d}t^2} = T_M - \frac{1}{G_H}T_L - C_M sgn\left(\frac{\mathrm{d}\delta_{Motor}}{\mathrm{d}t}\right) - \frac{C_S}{G_H}sgn\left(\frac{\mathrm{d}\delta_{sup}}{\mathrm{d}t}\right) \quad (15)$$

We assume perfect coupling between the motor and the load, i.e.,

$$\begin{aligned} \frac{\mathrm{d}\delta_{Motor}}{\mathrm{d}t} &= G_H \frac{\mathrm{d}\delta_{sup}}{\mathrm{d}t} \\ \frac{\mathrm{d}^2\delta_{Motor}}{\mathrm{d}t^2} &= G_H \frac{\mathrm{d}^2\delta_{sup}}{\mathrm{d}t^2} \end{aligned} \quad (16)$$

We plug these results into equation (15) and obtain

$$\left(G_H J_M + J_{Load}\right)\frac{\mathrm{d}^2\delta_{sup}}{\mathrm{d}t^2} = T_M - \frac{1}{G_H}T_L - \left(C_M + \frac{C_S}{G_H}\right)sgn\left(\frac{\mathrm{d}\delta_{sup}}{\mathrm{d}t}\right) \quad (17)$$

We use this knowledge to create a block diagram of the mechanical system submodule (Figure 12).

3.2.2 Mass Moment of Inertia of Load

In the previous section we have derived equations for the superimposed steering angle δ_{sup} as a function of the total inertia of the load J_{Load}. It was however not shown how to

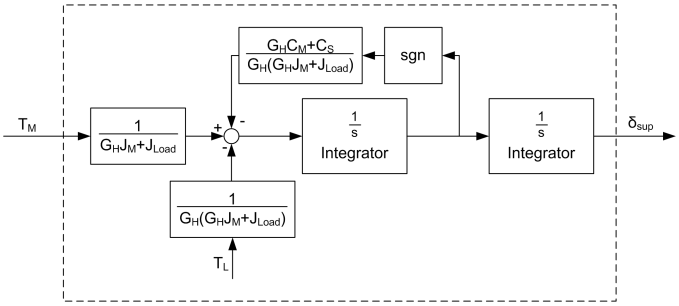

Figure 12: Mechanical system submodule.

calculate the actual inertia. This largely depends on the structure of the steering system. A rack-and-pinion steering system is used here. The pinion gear is attached to the steering column. Whenever the steering column rotates, the pinion turns as well, thus moving the rack (Figure 13).

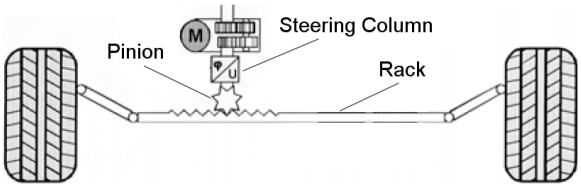

Figure 13: Rack-and-pinion steering system.

We now want to calculate the total inertia of the load. That is why we decompose the system into the PMSM, the steering column, the steering rack and the wheels (Figure 14). Only the steering column, the steering rack and the wheels are considered part of the load. Hence there are two inertias, namely the inertia J_S of the steering column and the inertia J_W of each of the front wheels. Besides, one has to consider the mass of the steering rack. J_S is already in the rotational frame of reference of the steering column. The other parameters are not. That is why they need to be transformed into this frame of reference.

We start with the inertia of the wheels J_W. Due to the gear ratio of the steering system, the wheels only have $1/G_S$ times the angular velocity of the steering column. Hence, according to [4], in order to transform J_W into the rotational frame of reference of the steering column, one has to divide J_M by G_S.

The steering rack with the mass m_r is subject to translatory motion. It needs to be

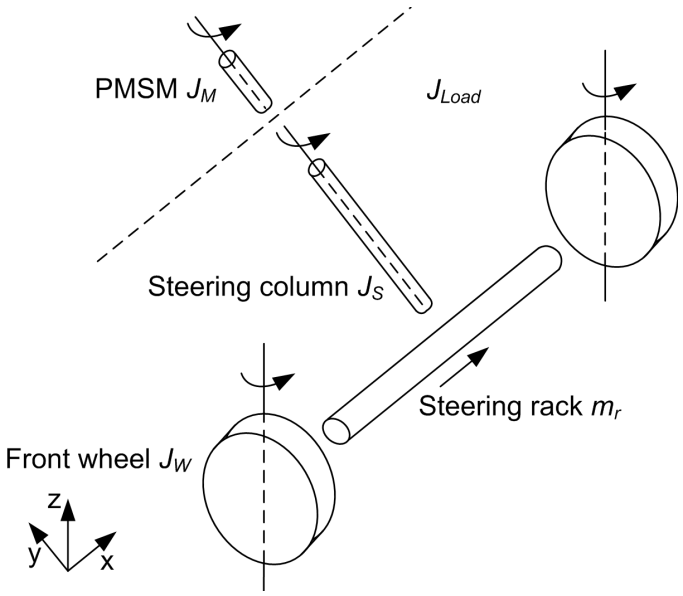

Figure 14: Decomposed steering system.

transformed into the rotational frame of reference of the steering column as well. This is done by multiplying m_r with the square of the pinion radius r_p. We add up all inertias transformed into the rotational frame of reference of the steering column. As a result the total inertia of the load is

$$J_{Load} = J_S + 2\frac{1}{G_S}J_W + {r_p}^2 m_r \tag{18}$$

3.3 Parameters of Low-Detail Steering Module

The parameters of the truck for the mechanical system submodule break down into the different parameters of the mechanical system submodule and the parameters required to calculate the inertia of the load.

3.3.1 Parameters of Mechanical System Submodule

As outlined above the load torque T_L is determined by the forces at the tire-road interface and the torque generated by the power steering system. We have measurements of the load torque T_L of a small truck, which will be integrated into the model. The Coulomb constant of the motor is $C_M = 0.032$ Nm and the Coulomb constant of the steering system is $C_S = 1.6$ Nm. The gear ratio of the steering system is $G_S = 14.4$ and the gear ratio of

the harmonic drive is $G_H = 50$. The motor has an inertia of $J_M = 2.61 * 10^{-6}$ kgm^2.

3.3.2 Parameters of Inertia of Load

The total inertia of the load system can be calculated using

$$J_{Load} = J_S + 2\frac{1}{G_S}J_W + {r_p}^2 m_r \tag{19}$$

We start with J_S. The steering column is modeled as a hollow cylinder with an inner radius of 14 mm, an outer radius of 24 mm and a moving mass of 2.5 kg (Figure 15). We plug in

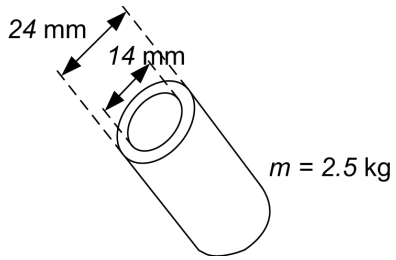

Figure 15: Inertia of steering column.

these number and obtain

$$J_S = \frac{1}{2} * 2.5 \text{ kg} \left[(24 \text{ mm})^2 - (14 \text{ mm})^2\right] = 4.75 * 10^{-4} \text{ kgm}^2 \tag{20}$$

We now look at J_W. The wheels are also modeled as cylinders. However, unlike the steering column, the wheels rotate around the the z-axis (compare Figure 14). This makes the calculation of the inertia more tedious. We derive the equation for the inertia of the wheels from the generic equation for the inertia of any rotating body. The inertia of a body rotating around an axis g is defined as the integral of the density ρ times the squared distance $a^2(g, x)$ to the axis g over the entire body, i.e.,

$$J = \iiint_K \rho a^2(g, x)\, \mathrm{d}V \tag{21}$$

We assume a constant density in the wheel. We can therefore move ρ out of the integral and obtain

$$J = \rho \iiint_K a^2(g, x)\, \mathrm{d}V \tag{22}$$

In order to make solving the integral easier, we will integrate merely over one eighth of the actual volume, as shown on the left of Figure 16. That is why the integral needs to be multiplied by eight in order to obtain the actual inertia. The integral in the x- and

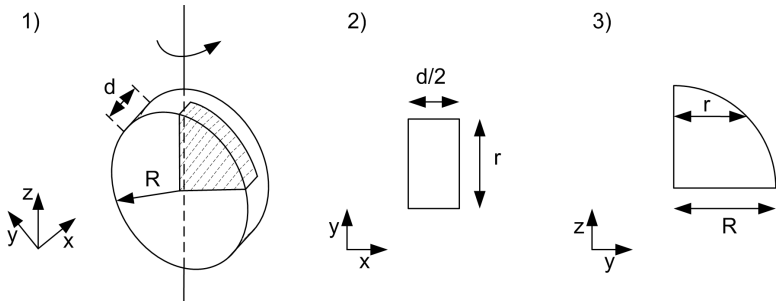

Figure 16: Inertia of wheel.

y-directions is

$$\int_0^{r(z)} \int_0^{\frac{d}{2}} a^2(g,x)\,\mathrm{d}x\,\mathrm{d}y = \int_0^{r(z)} \int_0^{\frac{d}{2}} \left(x^2+y^2\right)\,\mathrm{d}x\,\mathrm{d}y \tag{23}$$

In the next step we also integrate in z-direction. r is a function of z. The circle which is shown in Figure 16 on the right has the equation

$$r^2 + z^2 = R^2 \tag{24}$$

We also know that r as a function of z is

$$r(z) = \sqrt{R^2 - z^2} \tag{25}$$

Finally, we also integrate in the z-direction. Then the total inertia of the steering system is

$$J_W = 8\rho \int_0^R \int_0^{\sqrt{R^2-z^2}} \int_0^{\frac{d}{2}} \left(x^2+y^2\right)\,\mathrm{d}x\,\mathrm{d}y\,\mathrm{d}z \tag{26}$$

By solving this integral we obtain

$$\begin{aligned} J_W &= 8\rho \int_0^R \int_0^{\sqrt{R^2-z^2}} \left(\frac{1}{24}d^3 + \frac{1}{2}dy^2\right)\,\mathrm{d}y\,\mathrm{d}z \\ &= 8\rho \int_0^R \left(\frac{1}{24}d^3\sqrt{R^2-z^2} + \frac{1}{6}d\left(R^2-z^2\right)^{\frac{3}{2}}\right)\,\mathrm{d}z \\ &= 8\rho \left[\frac{1}{48}d^3\left(z\sqrt{R^2-z^2} + R^2 \arcsin\frac{z}{R}\right)\right]_0^R \end{aligned} \tag{27}$$

$$
\begin{aligned}
&+8\rho\left[\frac{1}{24}d\left(z\left(R^2-z^2\right)^{\frac{3}{2}}+\frac{3R^2z}{2}\sqrt{R^2-z^2}+\frac{3R^4}{2}\arcsin\frac{z}{R}\right)\right]_0^R\\
= \;& 8\rho\left[\frac{1}{48}d^3R^2\frac{\pi}{2}+\frac{1}{24}d\frac{3R^4}{2}\frac{\pi}{2}\right]
\end{aligned}
$$

The density of the wheels is $\rho = 3.1825 * 10^{-7}$ kg/mm^3, the radius is $R = 352$ mm and the width is $d = 232$ mm. Using these numerical values the value of the inertia is

$$
\begin{aligned}
J_W &= 2.546 * 10^{-6}\frac{\text{kg}}{\text{mm}^3}\left[\frac{1}{48}(232\text{ mm})^3(352\text{ mm})^2\frac{\pi}{2}+\frac{1}{24}232\text{ mm}\frac{3(352\text{ mm})^4}{2}\frac{\pi}{2}\right]\\
&= 1.0192\text{ kgm}^2 \qquad (28)
\end{aligned}
$$

Finally, we look at the steering rack. We know that the gear ratio of the steering system is $G_S = 14.4$. The mass of the steering rack is $m_r = 3.3$ kg and the pinion radius is $r_p = 7$ mm. We use all these values to calculate

$$J_{Load} = 0.1422\text{ kgm}^2 \qquad (29)$$

The initial steering parameters of the truck are summarized in Table 6.

Initial steering module		
G_S	gear ratio of steering system	14.4
G_H	gear ratio of harmonic drive	50
J_M	mass moment of inertia of PMSM rotor	$2.61 * 10^{-6}$ kgm^2
J_{Load}	total mass moment of inertia of load	0.1422 kgm^2
C_M	Coulomb constant of PMSM	0.032 Nm
C_S	Coulomb constant of steering system	1.6 Nm

Table 6: Parameters of initial steering module.

CHAPTER IV

ANALOG POSITION CONTROLLER

In this chapter we design an analog position controller to achieve a desired steering ratio defined as a function of the vehicle velocity. It is based on the model derived in Chapters 2 and 3. In Chapter 5 the analog position controller is augmented with a current controller. In Chapter 7 the position controller is taken to the digital domain.

4.1 Control Objective

The steering ratio is defined as the ratio of the steering angle δ_{SW} to the road-wheel angle δ_f. The control objective is to obtain a variable steering ratio as a function of the vehicle velocity v (Figure 17). Below the velocity $v_{min} = 4.167$ m/sec the ratio should be a constant

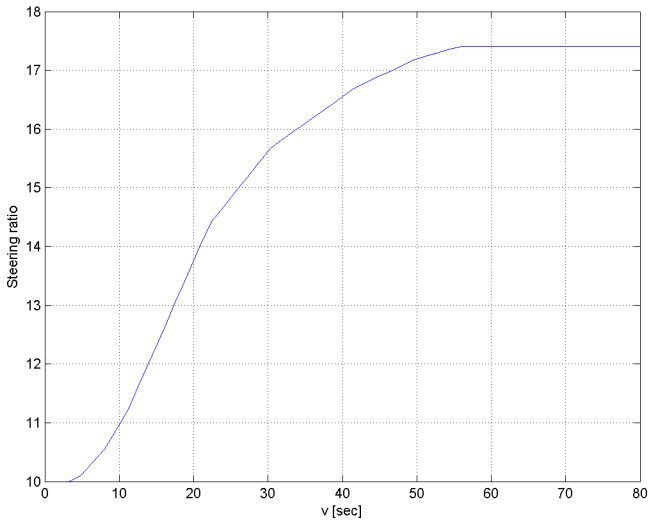

Figure 17: Desired steering ratio.

of 10 and above $v_{max} = 55.556$ m/sec the ratio should be 17.2. In between these two values, the ratio should increase as shown in Figure 17.

4.2 Overview of Analog Position Controller

4.2.1 Structure of Analog Position Controller

We use the control approach shown in Figure 18. There are two main parts to the controller.

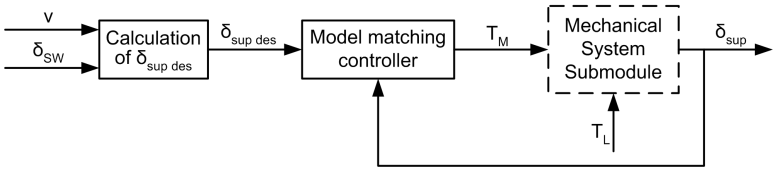

Figure 18: Structure of analog position controller.

First, one has to calculate the desired superimposed steering angle $\delta_{sup_{des}}$ from the vehicle velocity v and the steering wheel angle δ_{SW}. Second, one needs the actual controller to drive the actual superimposed steering angle δ_{sup} to the desired superimposed steering angle $\delta_{sup_{des}}$.

4.2.2 Calculation of Desired Superimposed Steering Angle

In order to obtain a desired steering ratio we first need to calculate the superimposed steering angle that is required to obtain the steering ratio shown in Figure 17. In Figure 19 we show a simplified representation of the steering module. There is a steering gear with a

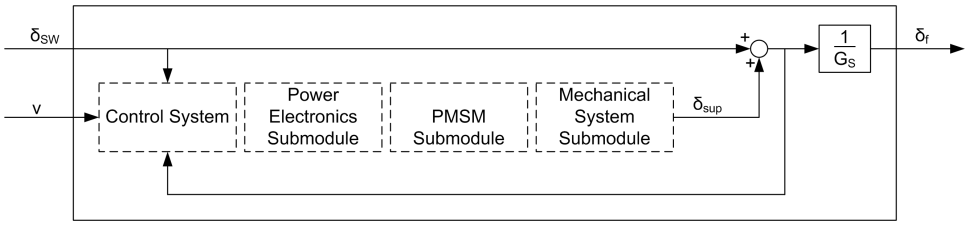

Figure 19: Simplified representation of steering module.

gear reduction of G_S in the system. That is why the actual road-wheel angle δ_f is the sum of the angle δ_{SW} imposed by the driver and the additional angle δ_{sup} from the superimposed steering system divided by G_S. Hence, the resulting road-wheel angle can be expressed as

$$\delta_f = \frac{1}{G_S}\left(\delta_{SW} + \delta_{sup}\right) \tag{30}$$

The steering ratio is the steering wheel angle divided by the road-wheel angle. The relationship between the desired superimposed steering angle $\delta_{sup_{des}}$ and the desired steering ratio r is therefore

$$r = \frac{\delta_{SW}}{\delta_f} = \frac{\delta_{SW}}{\frac{1}{G_S}\left(\delta_{SW} + \delta_{sup_{des}}\right)} \tag{31}$$

We solve this equation for the desired superimposed steering angle

$$\delta_{sup_{des}} = \delta_{SW}\left(\frac{G_S}{r} - 1\right) \tag{32}$$

4.3 Model Matching Controller

The design approaches used in classical control, e.g., root-locus or frequency-domain methods, are outward approaches. This implies that one first chooses among different control approaches and then tries to pick suitable parameters for a given controller to fulfill the control objectives. Hence, you start by choosing the internal compensators and then design the overall system such that design requirements are met. The problem with this method is that it is a trial-and-error approach. The inward approach, which is used here, goes exactly the other way. You first specify the overall transfer function that you would like to have and then choose a configuration. This allows you to take much greater influence on the behavior of the controlled system. One example for an inward approach is the model matching technique. You first specify the desired overall transfer function and then design a controller to achieve it. A detailed introduction to the inward approach and the model matching technique can be found in [2].

4.3.1 Desired Overall Transfer Function

The differential equation of the uncontrolled plant given in (17) is

$$\left(G_H J_M + J_{Load}\right)\frac{\mathrm{d}^2\delta_{sup}}{\mathrm{d}t^2} = T_M - \frac{1}{G_H}T_L - \left(C_M + \frac{C_S}{G_H}\right)sgn\left(\frac{\mathrm{d}\delta_{sup}}{\mathrm{d}t}\right) \tag{33}$$

This system is nonlinear because of the *sgn*-function. We do however plan to use model matching to design the controller. That is why we have to linearize the *sgn*-function (Figure 20). We have to make a tradeoff. If we choose the slope of the linearized function to be very large, we will have very high torque requirements for steep inputs. This might drive the

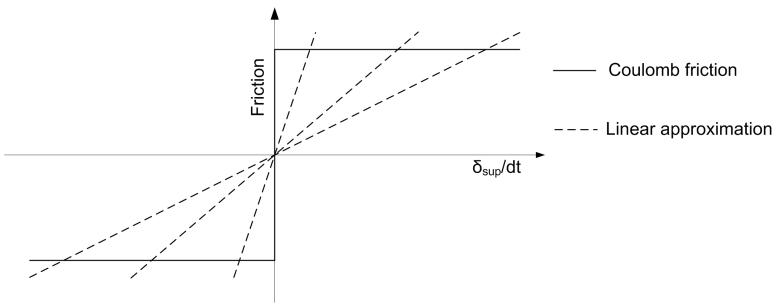

Figure 20: Linearization of Coulomb friction.

actuator into saturation. A small slope will result in slower rejection of Coulomb friction. Our priority here however is not to saturate the actuator. That is why we choose the linearization coefficient B to be rather small. Through simulation we have found out that determining the slope such that the error is zero for an angular velocity of $\dot{\delta}_{sup} = 50$ rad/s is a good choice. We therefore use

$$\begin{aligned} T_{Friction} &= B\frac{\delta_{sup}}{\mathrm{d}t} \\ \text{with } B &= \frac{C_M + \frac{C_S}{G_H}}{50\frac{rad}{s}} \end{aligned} \tag{34}$$

We apply this to equation (17) and thus linearize it to

$$(G_H J_M + J_{Load})\,\frac{\mathrm{d}^2\delta_{sup}}{\mathrm{d}t^2} = T_M - \frac{1}{G_H}T_L - B\frac{\mathrm{d}\delta_{sup}}{\mathrm{d}t} \tag{35}$$

If we set the load torque T_L to zero and summarize $G_H J_M + J_{Load} = C$, then the transfer function of this system from the motor torque T_M to the superimposed steering angle δ_{sup} is

$$G_1(s) = \frac{1}{Cs^2 + Bs} \tag{36}$$

We model the load torque as a disturbance and choose an appropriate transfer function of the controlled system from the desired superimposed steering angle $\delta_{sup_{des}}$ to the actual superimposed steering angle δ_{sup}. In choosing the desired transfer function we have to account for two things. First, we want tracking of the desired superimposed steering angle $\delta_{sup_{des}}$. Second, we intend to make use of a model matching approach in designing our controller. That is why the relative degree of the desired transfer function has to be at least

as large as the relative degree of the plant's transfer function. These considerations leave us with the desired transfer function

$$G_0(s) = \frac{\zeta {\omega_0}^2 s + {\omega_0}^3}{s^3 + \eta\omega_0 s^2 + \zeta {\omega_0}^2 s + {\omega_0}^3} \tag{37}$$

The numerical values that one chooses for η and ζ depend on the specific control objectives. We want to minimize the integral of time multiplied by velocity error (ITAE) as defined by

$$J_{ITAE} := \int_0^\infty t\,|e(t)|\;\mathrm{d}t \tag{38}$$

The choice of η and ζ for a ITAE zero-velocity-error optimal system is $\eta = 1.75$ and $\zeta = 3.25$.

Furthermore, we have to make a tradeoff at this point. The larger we choose the natural frequency ω_0, the faster the system. On the other hand, the larger ω_0, the bigger the control effort. We are however limited in the maximum torque that can be generated by the motor. That is why we choose ω_0 such that the system just meets the performance requirements in terms of responsiveness. We want the settling time to within 10% to be ≤ 0.02 sec. This is the case if $\omega_0 \leq 162$ sec^{-1}. That is why we choose $\omega_0 = 162$ sec^{-1}

The step response of the desired transfer function with the performance criteria is shown in Figure 21.

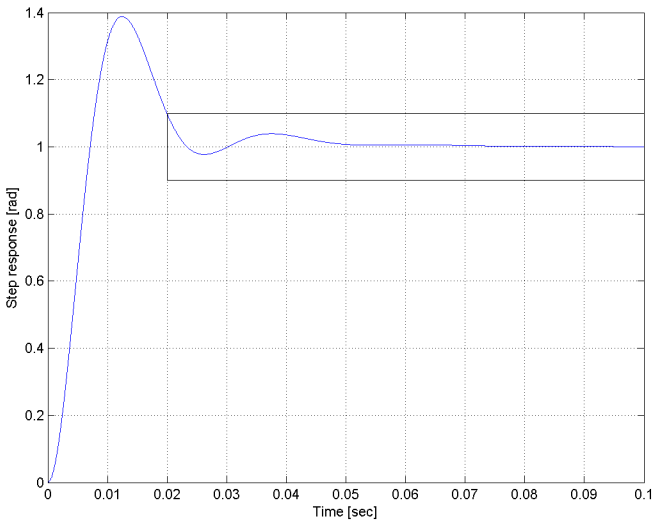

Figure 21: Step response of desired transfer function.

4.3.2 Control Design Using Model Matching

Now that we know both the plant transfer function $G_1(s)$ and the desired transfer function $G_0(s)$, we want to find compensators such that the transfer function of the resulting system equals $G_0(s)$. This is done using model matching. Unlike traditional outward approaches model matching allows us to place both poles and zeros, which is important as far as disturbance rejection and robustness are concerned. Since we have the load torque T_L, which may represent a significant disturbance, this property is highly important.

In order to achieve both pole and zero placement we need two-parameter compensation. We can assign different compensators to the reference input and the plant output and want the motor torque to be

$$T_M(s) = C_1(s)\delta_{sup_{des}}(s) - C_2(s)\delta_{sup}(s) \tag{39}$$

$C_1(s)$ is called the feedforward compensator and $C_2(s)$ is called the feedback compensator. Both functions can be defined by linear transfer functions, i.e.,

$$C_1(s) = \frac{L(s)}{A(s)} \quad C_2(s) = \frac{M(s)}{A(s)} \tag{40}$$

Since both $C_1(s)$ and $C_2(s)$ have the same denominator, we need to implement $A(s)$ only once. This also eliminates the problem of possible unstable pole-zero cancellation and reduces the number of integrators to a minimum (Figure 22). The prerequisites for model

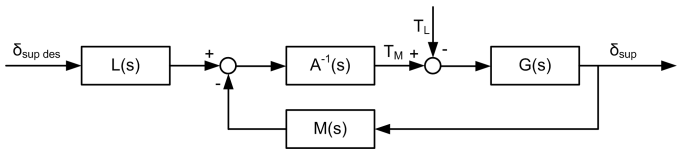

Figure 22: Plant with two-parameter model matching controller.

matching are that $G_1(s)$ is coprime and that $G_0(s)$ is implementable in the following sense.

- #1 Pole-zero excess inequality: The relative degree of the desired transfer function has to be greater or equal to the relative degree of the plant transfer function.

- #2 Retainment of non-minimum-phase zeros: All closed right hand plane zeros of

the plant transfer function $G_1(s)$ have to be retained in the desired transfer function $G_0(s)$.

- #3 Stability: The denominator of $G_0(s)$ is Hurwitz.

$G_1(s)$ is coprime and all conditions are met, because

- #1 Pole-zero excess inequality: $2 \geq 2$.
- #2 Retainment of non-minimum-phase zeros: $G_1(s)$ does not have any non-minimum-phase zeros.
- #3 Stability: Using the Routh test one can see that $D_0(s)$ is Hurwitz.

In order to calculate $L(s)$, $M(s)$ and $A(s)$ we need to go through several steps. We set up the general model matching condition. We introduce a Hurwitz polynomial $\bar{D}_p(s)$ to ensure that the resulting compensators are proper and good disturbance rejection is achieved. Finally, we solve the resulting equations.

We know that

$$\begin{aligned} G_1(s) &= \frac{N(s)}{D(s)} = \frac{1}{Cs^2 + Bs} \\ G_0(s) &= \frac{N_0(s)}{D_0(s)} = \frac{\zeta {\omega_0}^2 s + {\omega_0}^3}{s^3 + \eta\omega_0 s^2 + \zeta {\omega_0}^2 s + {\omega_0}^3} \end{aligned} \tag{41}$$

First we compute

$$\frac{G_0(s)}{N(s)} = \frac{N_0(s)}{D_0(s)N(s)} = \frac{\zeta {\omega_0}^2 s + {\omega_0}^3}{s^3 + \eta\omega_0 s^2 + \zeta {\omega_0}^2 s + {\omega_0}^3} =: \frac{N_p(s)}{D_p(s)} \tag{42}$$

$N_p(s)$ and $D_p(s)$ are coprime.

We want the actual transfer function to be identical to the desired transfer function, i.e.,

$$G_0(s) = \frac{N_p(s)N(s)}{D_p(s)} = \frac{L(s)N(s)}{A(s)D(s) + M(s)N(s)} \tag{43}$$

We now introduce a Hurwitz polynomial $\bar{D}_p(s)$ such that the following inequality

$$\deg D_p(s) \deg \bar{D}_p(s) \geq 2n - 1 \text{ where } n = \deg D(s) \tag{44}$$

is satisfied. Here $n = 2$ and $\deg D_p(s) = 3$. That is why it would be sufficient to choose the degree of $\bar{D}_p(s)$ as 0. We do however choose $\bar{D}_p(s)$ to be of degree 1, because this allows for better disturbance rejection as we will see in the following. Hence $\bar{D}_p(s)$ is

$$\bar{D}_p(s) = s + \alpha \text{ where } \alpha > 0 \tag{45}$$

We rewrite equation (43) using this $\bar{D}_p(s)$ and obtain

$$G_0(s) = \frac{N_p(s)N(s)}{D_p(s)} = \frac{N(s)\left[N_p(s)\bar{D}_p(s)\right]}{D_p(s)\bar{D}_p(s)} = \frac{N(s)L(s)}{A(s)D(s) + M(s)N(s)} \tag{46}$$

From this we can set up an equation for $L(s)$, which is

$$L(s) = N_p(s)\bar{D}_p(s) = \left(\zeta{\omega_0}^2 s + {\omega_0}^3\right)(s + \alpha) \tag{47}$$

We now also have an equation for $A(s)$ and $M(s)$.

$$\begin{aligned} A(s)D(s) + M(s)N(s) &= D_p(s)\bar{D}_p(s) \\ &= \left(s^3 + \eta\omega_0 s^2 + \zeta{\omega_0}^2 s + {\omega_0}^3\right)(s + \alpha) =: F(s) \end{aligned} \tag{48}$$

$F(s)$ is a polynomial of degree 4 and can therefore be expressed in the form

$$F(s) := D_p(s)\bar{D}_p(s) = F_4 s^4 + F_3 s^3 + F_2 s^2 + F_1 s + F_0 \tag{49}$$

$A(s)$ and $M(s)$ are polynomials of degree 2 and can be expressed as

$$\begin{aligned} A(s) &= A_2 s^2 + A_1 s + A_0 \\ M(s) &= M_2 s^2 + M_1 s + M_0 \end{aligned} \tag{50}$$

This is used to transform equation (48) into the matrix form

$$\begin{bmatrix} D_0 & N_0 & 0 & 0 & 0 & 0 \\ D_1 & N_1 & D_0 & N_0 & 0 & 0 \\ D_2 & N_2 & D_1 & N_1 & D_0 & N_0 \\ 0 & 0 & D_2 & N_2 & D_1 & N_1 \\ 0 & 0 & 0 & 0 & D_2 & N_2 \end{bmatrix} \begin{bmatrix} A_0 \\ M_0 \\ A_1 \\ M_1 \\ A_2 \\ M_2 \end{bmatrix} = \begin{bmatrix} F_0 \\ F_1 \\ F_2 \\ F_3 \\ F_4 \end{bmatrix} \tag{51}$$

Once we plug in the parameters this becomes

$$\begin{bmatrix} 0 & 1 & 0 & 0 & 0 & 0 \\ B & 0 & 0 & 1 & 0 & 0 \\ C & 0 & B & 0 & 0 & 1 \\ 0 & 0 & C & 0 & B & 0 \\ 0 & 0 & 0 & 0 & C & 0 \end{bmatrix} \begin{bmatrix} A_0 \\ M_0 \\ A_1 \\ M_1 \\ A_2 \\ M_2 \end{bmatrix} = \begin{bmatrix} {\omega_0}^3\alpha \\ {\omega_0}^3 + \zeta{\omega_0}^2\alpha \\ \zeta{\omega_0}^2 + \eta\omega_0\alpha \\ \eta\omega_0 + \alpha \\ 1 \end{bmatrix} \tag{52}$$

This system is underdetermined. Still, we want disturbance rejection. We will see later that step disturbances can only be rejected for $t \to \infty$ if $A_0 = 0$. That is why we choose $A_0 = 0$ and solve the linear equation for the remaining A_i and M_i.

$$\begin{aligned} A_0 &= 0 \\ A_1 &= \frac{1}{C}\left(\eta\omega_0 + \alpha - \frac{B}{C}\right) \\ A_2 &= \frac{1}{C} \\ M_0 &= {\omega_0}^3\alpha \\ M_1 &= {\omega_0}^3 + \zeta{\omega_0}^2\alpha \\ M_2 &= \zeta{\omega_0}^2 + \eta\omega_0\alpha - \frac{B}{C}\left(\eta\omega_0 + \alpha - \frac{B}{C}\right) \end{aligned} \tag{53}$$

We still have to determine the parameter α. We choose α in such a way that we can achieve disturbance rejection. The transfer function from the disturbance, i.e., load torque T_L, to the plant output δ_{sup} is

$$\begin{aligned} H(s) &:= \frac{\delta_{sup}(s)}{T_L(s)} = \frac{N(s)A(s)}{D_p(s)\bar{D}_p(s)} \\ &= \frac{s^2 + (\eta\omega_0 + \alpha)\, s}{(s^3 + \eta\omega_0 s^2 + \zeta{\omega_0}^2 s + {\omega_0}^3)\,(s + \alpha)} \end{aligned} \tag{54}$$

Now we can see why it was important to choose $A_0 = 0$. It is by doing this that we could ensure that $H(0) = 0$, i.e., disturbance rejection. The transfer function $H(s)$ has four poles: $s_1 = -59.01$, $s_2 = -112.24 + j243.82$, $s_3 = -112.24 - j243.82$ and $s_4 = -\alpha$. We choose $\alpha = 200$ so that the disturbance rejection is fast.

If we plug in all the vehicle parameters and previous results, we obtain the actual compensators

$$\begin{aligned} L(s) &= 8.5293 * 10^4 s^2 + 2.1310 * 10^7 s + 8.5031 * 10^8 \\ M(s) &= 1.4199 * 10^5 s^2 + 2.1310 * 10^7 s + 8.5031 * 10^8 \\ A(s) &= 7.0259 s^2 + 3.3970 * 10^3 s \end{aligned} \tag{55}$$

4.4 Evaluation of Analog Position Controller with Augmented Model

There are four major influences on the performance of the superimposed steering system:

- Curve radius
- Vehicle velocity
- Vehicle rate of acceleration/deceleration
- Steering wheel angle rate of acceleration/deceleration

We evaluate the controller by making use of two different scenarios in which we emphasize specific combinations of these influences. In order to do so we need to track the position of the vehicle in the x_1/x_2-plane. The velocity in the vehicle's coordinate frame is given by

$$\begin{aligned} v_{x_{1\,veh}} &= v \cos\beta \\ v_{x_{2\,veh}} &= v \sin\beta \end{aligned} \tag{56}$$

This is however in the vehicle's coordinate frame. If we want the velocity in the unmoved x_1/x_2-plane we have to add the angle between the vehicle main axis and the x_1-axis. If we assume that the vehicle points in x_1-direction at time 0, this angle can be obtained through integration of the vehicle yaw rate γ over time

$$\begin{aligned} v_{x_1} &= v \cos\left(\int_0^t \gamma \, \mathrm{d}t + \beta \right) \\ v_{x_2} &= v \sin\left(\int_0^t \gamma \, \mathrm{d}t + \beta \right) \end{aligned} \tag{57}$$

The actual position of the vehicle as a function of time can be obtained from this using

$$x_1 = \int_0^t \left[v \cos\left(\int_0^t \gamma \, \mathrm{d}t + \beta \right) \right] \mathrm{d}t \tag{58}$$

$$x_2 = \int_0^t \left[v \sin\left(\int_0^t \gamma \, \mathrm{d}t + \beta \right) \right] \mathrm{d}t$$

4.4.1 Scenario 1: Highway

When driving at high speed on the highway, the superimposed steering system should provide a steering ratio that is less direct than a conventional system. The highway environment is characterized by high speed and high curve radii combined with low accelerations of the vehicle and the steering wheel (Table 7).

curve radius r	high
vehicle velocity v	high
vehicle rate of acceleration/deceleration $\lvert\dot{v}\rvert$	low
steering wheel angle rate of acceleration/deceleration $\lvert\ddot{\delta}_{SW}\rvert$	low

Table 7: Characteristics of highway scenario.

We assess the behavior of the superimposed steering system by having the vehicle drive at constant velocity on a highway with two subsequent curves (Figure 23). The driver's

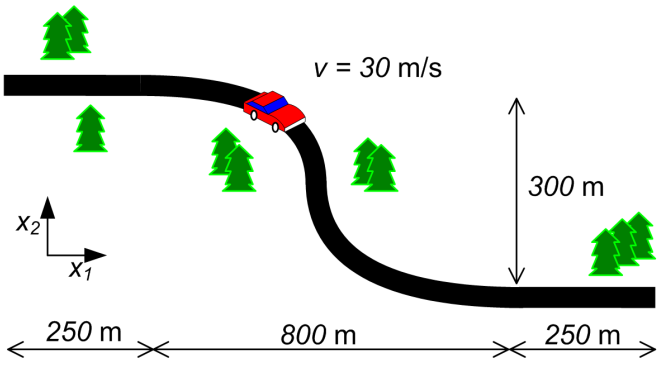

Figure 23: Road for highway scenario.

steering wheel angle has been selected such that the vehicle follows the given road. The exact steering wheel angle δ_{SW} over time can be seen in Figure 24.

The simulation results for this particular steering input and a vehicle velocity of $v = 30$ m/s can be seen in Figure 25. It is interesting to note that the shape of the curve of

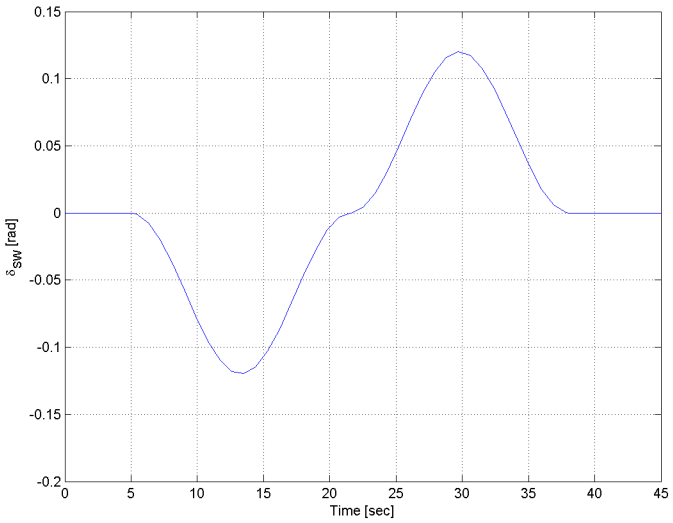

Figure 24: Steering input for highway scenario.

superimposed steering angle δ_{sup} is a scaled and mirrored version of the curve of the steering wheel angle δ_{SW}. This is no surprise, because the desired steering ratio at $v = 30$ m/s is above the mechanical ratio $G_S = 14.4$. Hence, the superimposed steering motor has to work against the steering wheel angle imposed by the driver in order for the steering system to be less direct.

In the lower diagram in Figure 25 we show the desired torque output of the electrical motor. One can see that the absolute value of the torque output of the electric motor always remains below 0.1 Nm. Hence the torque output is feasible for our choice of motor, which has a nominal torque of about 0.5 Nm. We also see some small oscillations of the torque output for $t \geq 38$ sec. In these instances the desired superimposed steering angle is $\delta_{sup} = 0$ rad. The oscillations are caused by the Coulomb friction in the steering system. As one can see from the diagram of the superimposed steering angle δ_{sup}, these oscillations are however so small that they represent no limitation to the performance of the system.

The above mentioned simulation results show that the controller gives satisfying results that correspond to what one would logically expect. The most important performance measure for the controller is however its ability to achieve the specific steering ratio as a function of vehicle velocity. The vehicle drives at 30 m/s. According to our control objective

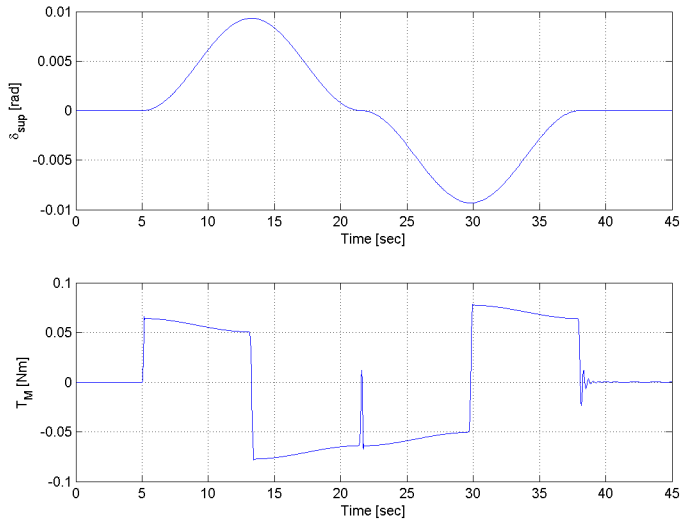

Figure 25: Superimposed steering angle and torque output for highway scenario.

(Figure 17) our desired steering ratio at this speed is 15.61.

The actual steering ratio is shown in Figure 26. The ratio is zero for $t \leq 5$ sec and $t \geq 38$ sec. Moreover, there is a peak around $t \approx 22$ sec. These phenomena are not due to the controller, but to the definition of the steering ratio. The road-wheel angle crosses zero at these time instances. Since the steering ratio is defined as the steering wheel angle divided by the road-wheel angle, the steering ratio becomes either zero or infinite at these instances. Considering this fact we can conclude that the actual steering ratio corresponds to the desired ratio of 15.61. The system also is sufficiently fast, as the desired steering ratio is generally reached within one third of a second.

Based on this first scenario we conclude that the analog position controller is valid for scenarios involving a high and constant velocity, high curve radii and low rates of acceleration of the steering wheel angle.

4.4.2 Scenario 2: Inner City

In the city the vehicle will drive at lower speeds than on the highway. As a result we will generally want a more direct steering ratio than the one given by the mechanical ratio G. As a result the superimposed steering angle δ_{sup} should now run in parallel to the steering

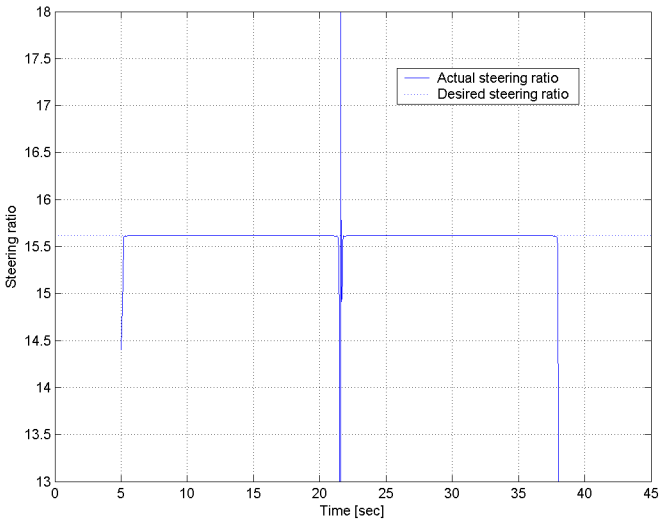

Figure 26: Desired and actual steering ratio for highway scenario.

wheel angle δ_{SW} and not in the exactly opposite direction as in the highway scenario.

Moreover, the torque requirements should increase as we now have higher rates of acceleration and smaller curve radii resulting in higher and more rapidly changing superimposed steering angles. The important characteristics of the inner city scenario have been summarized in Table 8.

curve radius r	small
vehicle velocity v	low
vehicle rate of acceleration/deceleration $\lvert\dot{v}\rvert$	high
steering wheel angle rate of acceleration/deceleration $\left\lvert\ddot{\delta}_{SW}\right\rvert$	high

Table 8: Characteristics of inner city scenario.

The inner city scenario comprises three straight sections with two curves in between (Figure 27). Unlike the highway scenario we accelerate and decelerate the vehicle. The driver decelerates the car when entering the first curve. The car is then accelerated as the vehicle leaves the curve. The same procedure is repeated for the second curve. Hence, we now have a variable vehicle velocity v. Since the desired steering ratio is a function of v, it will now change as a function of time. This is a new challenge that we did not face in the first scenario. The steering and velocity inputs for the inner city scenario are shown in

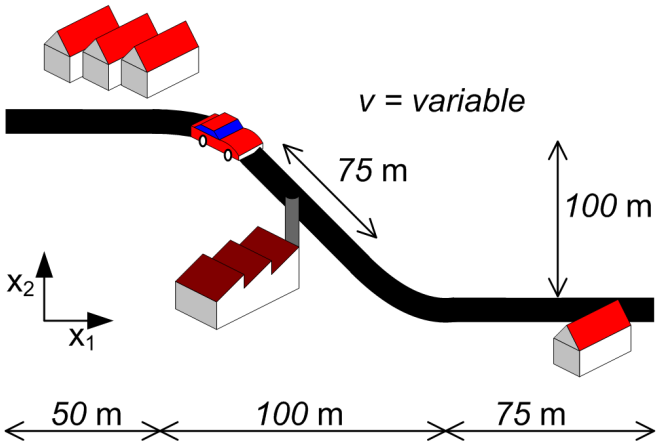

Figure 27: Road for city city scenario.

Figure 28.

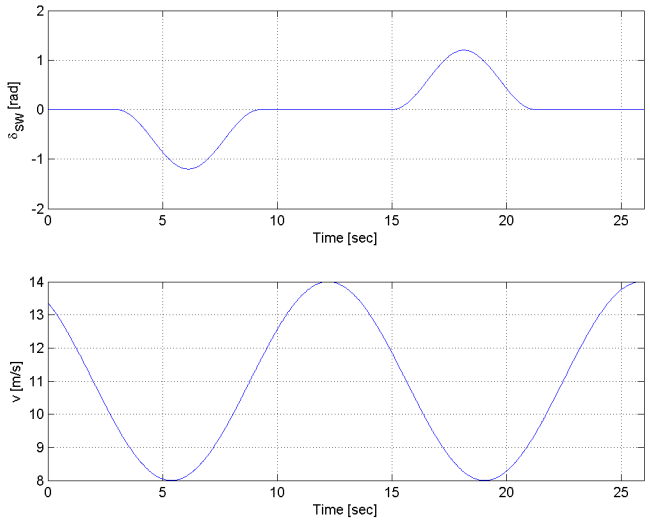

Figure 28: Steering and velocity inputs for inner city scenario.

The simulation results for the superimposed steering angle δ_{sup} and the torque output T_M are shown in Figure 29. Unlike the highway scenario, the δ_{sup} now runs in parallel with the steering wheel angle δ_{SW}. This is because the vehicle drives at relatively low speed and the superimposed steering system therefore increases the angle chosen by the driver in order to provide a more direct ratio between δ_{SW} and the δ_f.

The torque output for this scenario is within a feasible range in terms of the actuator

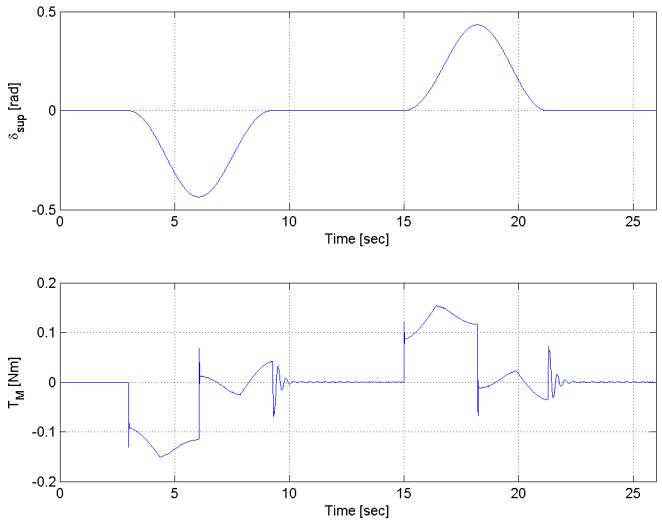

Figure 29: Superimposed steering angle and torque output for inner city scenario.

performance. Like in the previous example we experience some oscillations if δ_{sup} approaches zero. As mentioned above these are due to Coulomb friction and represent no limitation to the performance of the system.

The primary performance criterion is the relationship between the desired and the actual steering ratio (Figure 30). As one can see, the curves run mostly on top of each other. If they do not, then it is because δ_{sup} is very close to or equal to zero. As outlined above, the actual steering ratio is not defined in these instances. Considering this, we can conclude that the actual steering ratio follows the desired ratio very well.

Based on this second scenario we conclude that the analog position controller is also valid for scenarios involving variable velocities, low curve radii and high rates of acceleration of the steering wheel angle.

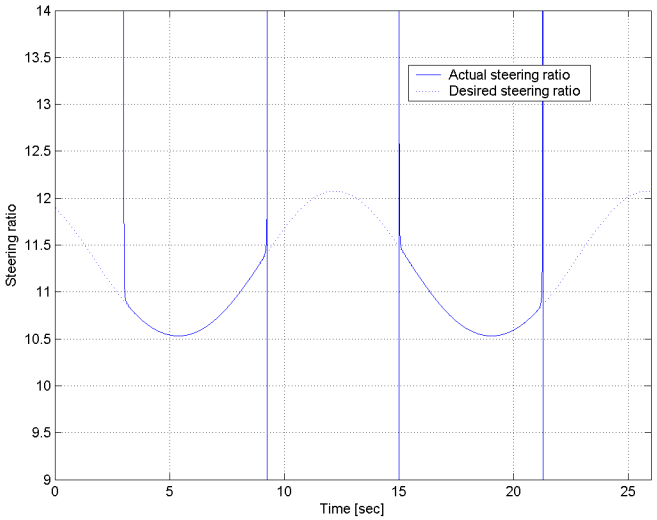

Figure 30: Desired and actual steering ratio for inner city scenario.

CHAPTER V

FINAL MODEL - HIGH-DETAIL STEERING MODULE

We now increase the level of detail in the steering module that we first described in Chapter 3. We do so by modeling the dynamics of the electric motor.

5.1 Structure of High-Detail Steering Module

The high-detail steering module is different from the low-detail steering module in that we now model the internal dynamics of the actuator. Hence, we no longer assume torque being a direct output of the controller. Instead, we now assume that the output of the controller is voltage, which is fed to the permanent-magnet synchronous motor with sinusoidally distributed stator windings. We do not model the dynamics of the power electronics here. Hence, the output of the controller in our model is the voltage $\underline{v}$ as shown in Figure 31.

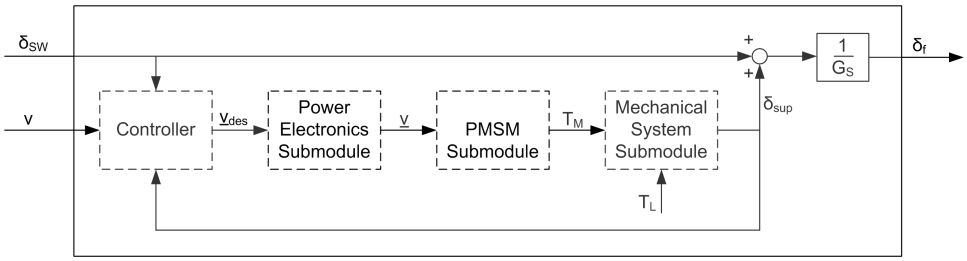

Figure 31: High-detail steering module.

5.2 Permanent-Magnet Synchronous Motor Submodule

The physical system has three phases. Due to the fact that these are wye-connected, it is however sufficient to model currents and voltages along two axes. Hence, the equations for the three phases are strongly coupled. That is why we start by modeling the three phases of the physical system in the abc frame of reference of the stator. We then transform these equations to the qd frame of reference of the rotor allowing easier modeling.

5.2.1 Equations in abc Frame of Reference

A brushless, permanent-magnet synchronous motor with sinusoidally distributed stator windings is to be used for the superimposed steering system. Compared to a conventional, brush-commutated motor, the brushless motor offers higher reliability and less frictional loss. Since we use sinusoidally distributed stator windings, we also have sinusoidal magnetics. This refers to the magnetic flux due to the phase currents. There are also permanent-magnet synchronous motors with trapezoidal magnetics on the market. Each of the two approaches has specific advantages and disadvantages. According to [10] trapezoidal magnetics require less precise control sensors and are simpler to implement. Sinusoidal magnetics on the other hand are more complex, but do allow for much more precise positioning of the motor. Since this aspect is crucial in a superimposed steering system, we choose sinusoidal magnetics.

The derivation of the equations is adapted from [12]. The voltage equations for all three phases of the PMSM are

$$\begin{bmatrix} v_a(t) \\ v_b(t) \\ v_c(t) \end{bmatrix} = \begin{bmatrix} R & 0 & 0 \\ 0 & R & 0 \\ 0 & 0 & R \end{bmatrix} \begin{bmatrix} i_a(t) \\ i_b(t) \\ i_c(t) \end{bmatrix} + \begin{bmatrix} \dot{\lambda}_a(t) \\ \dot{\lambda}_b(t) \\ \dot{\lambda}_c(t) \end{bmatrix} \tag{59}$$

The indices a, b and c represent the three stator phases. $v_a(t)$, $v_b(t)$ and $v_c(t)$ are the phase voltages, $i_a(t)$, $i_b(t)$ and $i_c(t)$ are the phase currents and $\lambda_a(t)$, $\lambda_b(t)$ and $\lambda_c(t)$ are the flux linkages. R is the resistance which is assumed to be the same in all phases. The flux, which is shifted by $2\pi/3$ between each of the three phases, is

$$\begin{bmatrix} \lambda_a(t) \\ \lambda_b(t) \\ \lambda_c(t) \end{bmatrix} = \begin{bmatrix} L & -M & -M \\ -M & L & -M \\ -M & -M & L \end{bmatrix} \begin{bmatrix} i_a(t) \\ i_b(t) \\ i_c(t) \end{bmatrix} + \lambda_m \begin{bmatrix} \sin\left(\theta(t)\right) \\ \sin\left(\theta(t) - \frac{2\pi}{3}\right) \\ \sin\left(\theta(t) + \frac{2\pi}{3}\right) \end{bmatrix} \tag{60}$$

where $\theta(t)$ is the rotor position, L the stator self-inductance, M is the stator-to-stator mutual inductance, λ_m is the magnitude of the flux created by the permanent magnets, and N is the number of poles. We assume an ideal coupling between the superimposed steering angle δ_{sup}, the gear set and the rotor position θ. That is why $\theta = G_H N \delta_{sup}$. We

plug this into equation (60) and get

$$\begin{bmatrix} \lambda_a(t) \\ \lambda_b(t) \\ \lambda_c(t) \end{bmatrix} = \begin{bmatrix} L & -M & -M \\ -M & L & -M \\ -M & -M & L \end{bmatrix} \begin{bmatrix} i_a(t) \\ i_b(t) \\ i_c(t) \end{bmatrix} + \lambda_m \begin{bmatrix} \sin\left(G_H N \delta_{sup}\right) \\ \sin\left(G_H N \delta_{sup} - \frac{2\pi}{3}\right) \\ \sin\left(G_H N \delta_{sup} + \frac{2\pi}{3}\right) \end{bmatrix} \tag{61}$$

The generated torque can be calculated from

$$\begin{aligned} T_M(t) &= N\lambda_m \Big[i_a(t) \cos\left(G_H N \delta_{sup}(t)\right) + i_b(t) \cos\left(G_H N \delta_{sup}(t) - \frac{2\pi}{3}\right) \\ &\quad + i_c(t) \cos\left(G_H N \delta_{sup}(t) + \frac{2\pi}{3}\right) \Big] \end{aligned} \tag{62}$$

We wye-connect the three phases. The phase voltages and currents must therefore add up to zero, i.e.,

$$\begin{aligned} v_a(t) + v_b(t) + v_c(t) &= 0 \\ i_a(t) + i_b(t) + i_c(t) &= 0 \end{aligned} \tag{63}$$

We plug this into equation (61) and obtain

$$\begin{bmatrix} \lambda_a(t) \\ \lambda_b(t) \\ \lambda_c(t) \end{bmatrix} = \begin{bmatrix} L' & 0 & 0 \\ 0 & L' & 0 \\ 0 & 0 & L' \end{bmatrix} \begin{bmatrix} i_a(t) \\ i_b(t) \\ i_c(t) \end{bmatrix} + \lambda_m \begin{bmatrix} \sin\left(G_H N \delta_{sup}\right) \\ \sin\left(G_H N \delta_{sup} - \frac{2\pi}{3}\right) \\ \sin\left(G_H N \delta_{sup} + \frac{2\pi}{3}\right) \end{bmatrix} \text{ with } L' = L + M \tag{64}$$

5.2.2 Equations in qd Frame of Reference

Equations (62) and (64) depend on the superimposed steering angle δ_{sup}. This dependence can be eliminated by transforming from the stator to the rotor frame. This allows for easier control of torque output and electrical losses. The change for wye-connected phases, the so-called Park's transformation, is given by multiplication with the matrix $\underline{P}$. A detailed analysis of this transformation can be found in [13]. The matrix is

$$\underline{P} = \sqrt{\frac{2}{3}} \begin{bmatrix} \cos\left(G_H N \delta_{sup}\right) & \cos\left(G_H N \delta_{sup} - \frac{2\pi}{3}\right) & \cos\left(G_H N \delta_{sup} + \frac{2\pi}{3}\right) \\ \sin\left(G_H N \delta_{sup}\right) & \sin\left(G_H N \delta_{sup} - \frac{2\pi}{3}\right) & \sin\left(G_H N \delta_{sup} + \frac{2\pi}{3}\right) \end{bmatrix} \tag{65}$$

The inverse transformation from the qd to the abc frame of reference is given by multiplication with

$$\underline{Q} = \sqrt{\frac{2}{3}} \begin{bmatrix} \cos\left(G_H N \delta_{sup}\right) & \sin\left(G_H N \delta_{sup}\right) \\ \cos\left(G_H N \delta_{sup} - \frac{2\pi}{3}\right) & \sin\left(G_H N \delta_{sup} - \frac{2\pi}{3}\right) \\ \cos\left(G_H N \delta_{sup} + \frac{2\pi}{3}\right) & \sin\left(G_H N \delta_{sup} + \frac{2\pi}{3}\right) \end{bmatrix} \tag{66}$$

We apply Park's transformation to equations (59), (61) and (64). The resulting set of equations describing the internal dynamics of the PMSM in the qd frame of reference is

$$\begin{aligned} L'\dot{i}_q(t) &= -N\left(\lambda_m{}' + L' i_d(t)\right) G_H \dot{\delta}_{sup}(t) - R i_q(t) + v_q(t) \\ L'\dot{i}_d(t) &= N L' i_q(t) G_H \dot{\delta}_{sup}(t) - R i_d(t) + v_d(t) \\ T_M(t) &= N \lambda_m{}' i_q(t) \\ &\quad \text{with } \lambda_m{}' = \sqrt{\frac{3}{2}} \lambda_m \end{aligned} \tag{67}$$

The above transformation and the set of equations allow calculating the desired quadrature-axis current $i_{q_{des}}$ and the desired direct-axis current $i_{d_{des}}$. In the physical system we do however only have phase currents and voltages. That is why in the actual controller we have to transform back from the qd frame of reference to the abc frame of reference. This is done using matrix $\underline{Q}$ and has not been modeled here.

The resulting PMSM submodule is shown in Figure 32.

5.3 Power Electronics Submodule

In Figure 33 we show how the currents in the individual phases look like in the stationary case, i.e., for constant torque output. As one can see the phase currents are sinusoidal in the stationary case. That is why the desired phase voltages $v_{a_{des}}$, $v_{b_{des}}$ and $v_{c_{des}}$ are generally also modified sinusoids. Hence, we need to create sinusoidal voltages in the power electronics. We do however merely have the constant supply voltage of 12 V from the vehicle's battery. That is why we use a pulse-width modulated (PWM) inverter to generate sinusoidal curves. The current to the three motor terminals is controlled by six semiconductor switches (Figure 34).

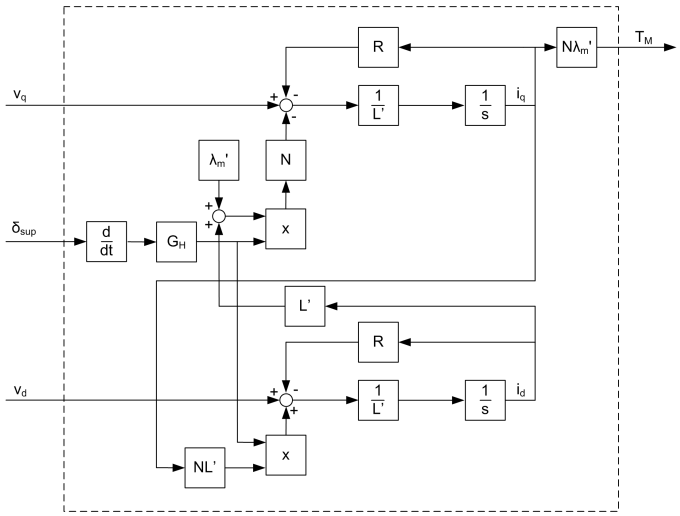

Figure 32: PMSM submodule.

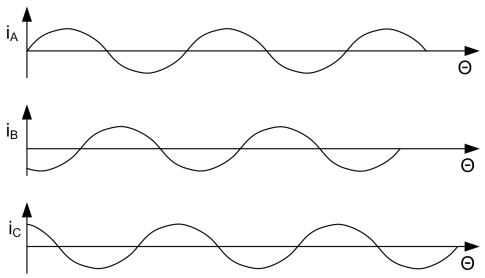

Figure 33: Current in individual phases of PMSM.

Since we only have the constant supply voltage, all we can do is switch the voltage in either phase to -12 V, 0 V or 12 V. However, the PWM is extremely fast compared to the dynamics of the rest of the system. By rapidly switching between the three possible states in each phase, we can generate any average voltage between -12 V and 12 V. Since the PWM is much faster than the rest of the system, the motor will react as if there were no switching and just a constant voltage.

Since the focus here is on the implementation of a superimposed steering system and not on the dynamics of power electronics, we do not model the system down to the switching of the individual semiconductors. Instead we assume that the power electronics have a transfer function of 1, i.e., the PWM produces exactly the voltages demanded by the inner controller (Figure 35). A detailed analysis of the PWM can be found in [12].

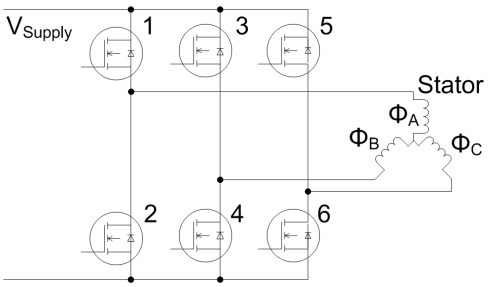

Figure 34: Pulse-width modulated inverter.

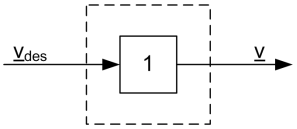

Figure 35: Power electronics submodule.

5.4 Parameters of High-Detail Steering Module

We use a PMSM with three pole pairs. Therefore $N = 3$. We determine the resistance R and the inductance L' by averaging the line-to-line resistance and inductance respectively and dividing the results by two. Hence, we obtain that $R = 83.67$ mΩ and $L' = 42.73$ μH. The flux magnitude is $\lambda_m = 5.096$ mWb.

The steering parameters of the high-detail steering module are summarized in Table 9.

Steering module		
N	PMSM number of pole pairs	3
L'	PMSM inductance	42.73 μH
R	PMSM resistance	83.67 mΩ
λ_m	flux magnitude	5.096 mWb

Table 9: Parameters of high-detail steering module.

CHAPTER VI

ANALOG CURRENT CONTROLLER

In the last chapters we merely considered a position controller that had torque as a direct ouput. In this chapter we augment the existing position controller with an inner control loop for controlling the current i_q and i_d.

6.1 Control Objective

Since we already have an analog position controller, the current controller depends primarily on the structural integration of the position controller with the current controller. The structure of the outer position controller and the inner current controller is shown in Figure 36. The input to the current controller is the desired torque output $T_{M_{des}}$ and the outputs

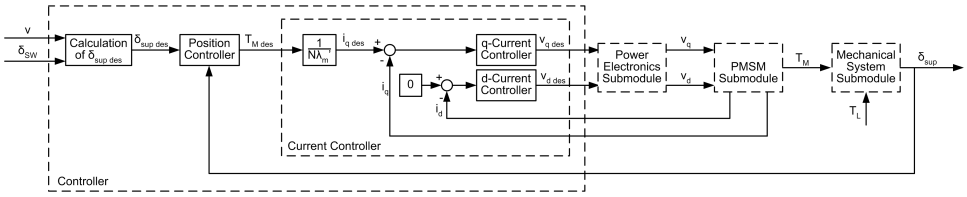

Figure 36: Control structure.

are the voltages v_q and v_d. The control objective therefore consists of determining v_q and v_d such that the actual torque output T_M reaches the desired torque output $T_{M_{des}}$ as fast as possible. At the same time we want to minimize electrical losses in the motor.

We thus need to control two currents. The quadrature-axis current i_q produces actual torque. Hence, we want to control i_q as a function of the desired torque output $T_{M_{des}}$. The direct-axis current i_d on the other hand does not produce torque, but merely results in electrical losses. That is why we always want to drive it to zero. We use feedback linearization in combination with PI controllers to determine the voltages v_q and v_d.

6.2 Feedback Linearization and PI Controllers

This controller is used to drive the actual quadrature-axis current i_q to the desired quadrature-axis current $i_{q_{des}}$. Since we have shown in equation (64) that torque is a linear function of i_q, the desired quadrature-axis current $i_{q_{des}}$ can be calculated from the desired torque output $T_{M_{des}}$ using

$$i_{q_{des}} = \frac{T_{M_{des}}}{N\lambda_m{}'} \tag{68}$$

In the literature, e.g., [9], it is mostly suggested using PI compensators for both the quadrature-axis and the direct-axis currents. We take a different approach here allowing for better decoupling. We first linearize the plant using feedback linearization and then apply standard PI control.

6.2.1 Feedback Linearization

The coupled equations for i_q and i_d have been given in equation (67) by

$$\begin{aligned} \dot{i}_q(t) &= \underbrace{-\frac{N}{L'}\left(\lambda_m{}' + L'i_d(t)\right) G_H\dot{\delta}_{sup}(t)}_{\alpha_1(i_d)} - \frac{R}{L'}i_q(t) + \frac{1}{L'}v_q(t) \\ \dot{i}_d(t) &= \underbrace{Ni_q(t)G_H\dot{\delta}_{sup}(t)}_{\alpha_2(i_q)} - \frac{R}{L'}i_d(t) + \frac{1}{L'}v_d(t) \end{aligned} \tag{69}$$

This can be rewritten as

$$\begin{bmatrix} \dot{i}_q \\ \dot{i}_d \end{bmatrix} = \begin{bmatrix} \alpha_1(i_d) \\ \alpha_2(i_q) \end{bmatrix} + \begin{bmatrix} -\frac{R}{L'} & 0 \\ 0 & -\frac{R}{L'} \end{bmatrix} \begin{bmatrix} i_q \\ i_d \end{bmatrix} + \frac{1}{L'} \begin{bmatrix} v_q \\ v_d \end{bmatrix} \tag{70}$$

The nonlinear terms in equation (70) are $\alpha_1(x)$ and $\alpha_2(x)$. The nonlinearities and the control terms v_q and v_d respectively appear together as a sum. That is why the effect of the nonlinearities can be easily canceled using the control algorithm

$$\begin{aligned} v_q &= -L'\alpha_1(i_d) + u_q \\ v_d &= -L'\alpha_2(i_q) + u_d \end{aligned} \tag{71}$$

Hence the control inputs v_q and v_d comprise two components. First, $L'\alpha_1(i_d)$ and $L'\alpha_2(i_q)$ are used to cancel the nonlinearities. Second, u_q and u_d are used to control the remaining linearized plant.

6.2.2 PI Controllers

With the cancellation of the nonlinearities the equations of the plant transform to

$$\begin{aligned} \dot{i}_q &= -\frac{R}{L'} i_q + \frac{1}{L'} u_q \\ \dot{i}_d &= -\frac{R}{L'} i_d + \frac{1}{L'} u_d \end{aligned} \tag{72}$$

PI control is the most common approach here. The transfer function of a PI controller is

$$G_{PI} = K_P + K_I \frac{1}{s} \tag{73}$$

We take the s-transform of equation (72) and plug in the transfer function of a PI controller for u_q and u_d. With that we obtain the transfer function of the linearized controlled plant, which is

$$G_2(s) = \frac{\frac{K_P}{L'} \left(s + \frac{K_I}{K_P} \right)}{s^2 + \frac{R+K_P}{L'} s + \frac{K_I}{L'}} \tag{74}$$

We now need to determine the parameters K_P and K_I. In doing so we must account for two performance requirements.

- #1 Tracking: We implemented the position controller to track ramp reference inputs. That is why in order to obtain suitable performance we also need tracking in the current controller. Perfect tracking is achieved if $G'(0) = 1$. This cannot be obtained here. We can however obtain approximate tracking by choosing K_P such that $\frac{K_P}{L'} \approx \frac{R+K_P}{L'}$. We should therefore choose $K_P > R$.

- #2 No overshoot: In order not to cause oscillations in the system output, we choose a damping ratio $\zeta \geq 1$ with a denominator of the form $s^2 + 2\zeta\omega_1 s + {\omega_1}^2$.

Obviously the current controller must be faster than the position controller. We chose the natural frequency $\omega_0 = 162$ sec^{-1} for the outer controller. That is why we now choose $\omega_1 = 400$ sec^{-1} for the current controller. From this we can determine $K_I = 6.8368$. Moreover, we choose $K_P = 0.25$, which is siginificantly larger than $R = 0.08367\ \Omega$. This corresponds to a damping ratio $\zeta = 9.761$.

6.3 Evaluation of Analog Current Controller with Final Model

We use the same scenarios as in Chapter 4 to assess the performance of the inner controller. By comparing the results from this chapter and Chapter 4 we can thus find out how the inner controller affects the performance of the overall system, i.e., to what extent the system is slowed down by the internal dynamics of the PMSM.

6.3.1 Scenario 1: Highway

The steering input, the velocity profile and all other parameters are identical to those used in Subsection 4.4.1. That is why they are not repeated here. However, we also simulate the internal dynamics of the PMSM and the inner controller.

The simulated superimposed steering angle δ_{sup} and the torque output T_M are shown in Figure 37.

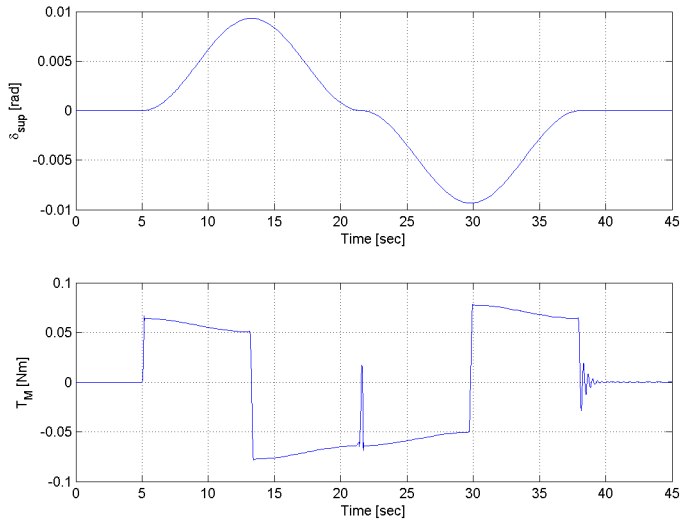

Figure 37: Superimposed steering angle and torque output for highway scenario.

We assess the performance by comparing Figure 37 with Figure 25. As one can see the inner controller compensates for the internal dynamics of the PMSM such that there are no apparent differences in the torque output and the superimposed steering angle between the two simulations.

In the next step we assess if the inner and outer controller still allow us to maintain the desired steering ratio (Figure 38). We can once again conclude that the combination of

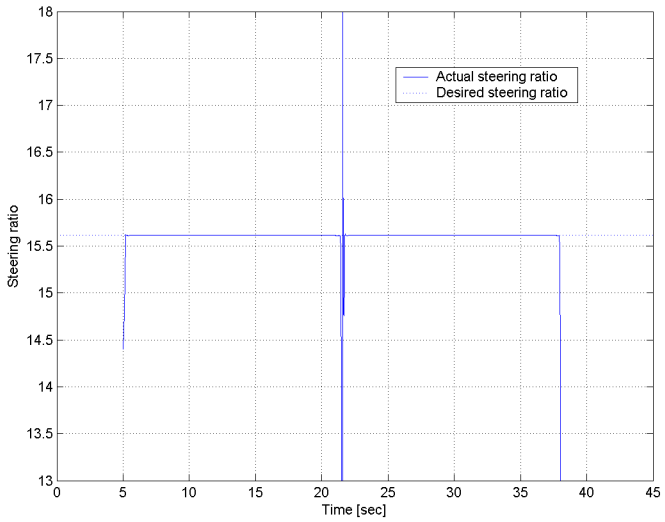

Figure 38: Desired and actual steering ratio for highway scenario.

the inner and the outer controller gives satisfying results. The curve of the steering ratio is practically identical to the one from Subsection 4.4.1.

Finally, in considering the internal dynamics of the PMSM it is essential to look at the phase currents. This is because the linear relationship between torque and the quadrature-axis current is only valid within a certain region. Moreover, exceedingly high phase currents will result in large power dissipation ultimately heating up and damaging the motor. That is why we want the current to remain below 15 A at all times. We show the currents in the three phases of the PMSM in Figure 39. As one can see the currents in the three phases are always below the maximum continuous current of 18 A.

6.3.2 Scenario 2: Inner City

Parameters and inputs are the same as in Subsection 4.4.2. As in the previous subsection we now model the internal dynamics of the PMSM and apply the inner controller to compare the results to those obtained in Chapter 4.

This results in the superimposed steering angle δ_{sup} and torque output T_M shown in

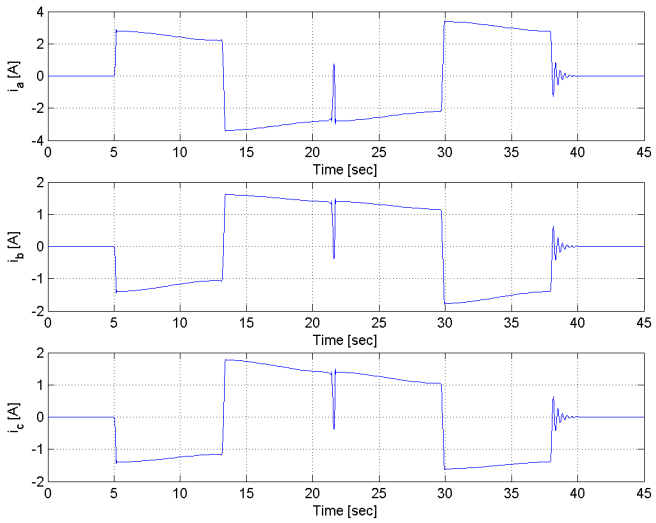

Figure 39: Phase currents for highway scenario.

Figure 40. As one can see both the superimposed steering angle and the torque output are virtually identical to those calculated in Subsection 4.4.2. Moreover, the actual steering ratio follows the desired steering ratio very well (Figure 41). Since the phase currents are also within an acceptable range (Figure 42), the combination of the outer and the inner controller is a suitable approach for reaching the control objective using continuous-time controllers. We have shown that the controllers are suitable if applied to a model comprising the internal dynamics of the PMSM.

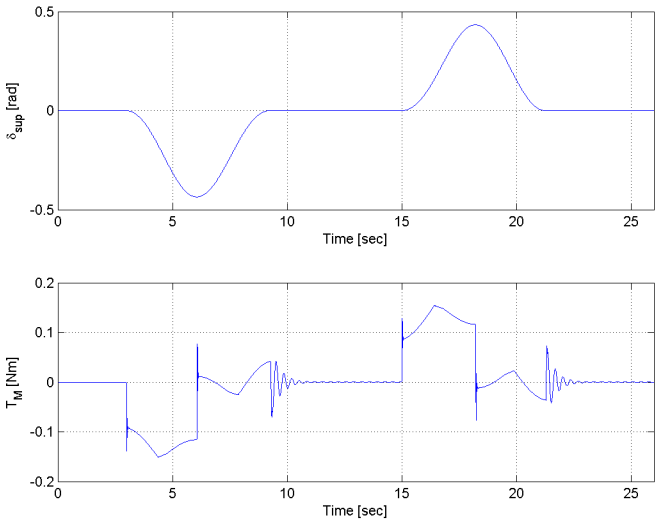

Figure 40: Superimposed steering angle and torque output for inner city scenario.

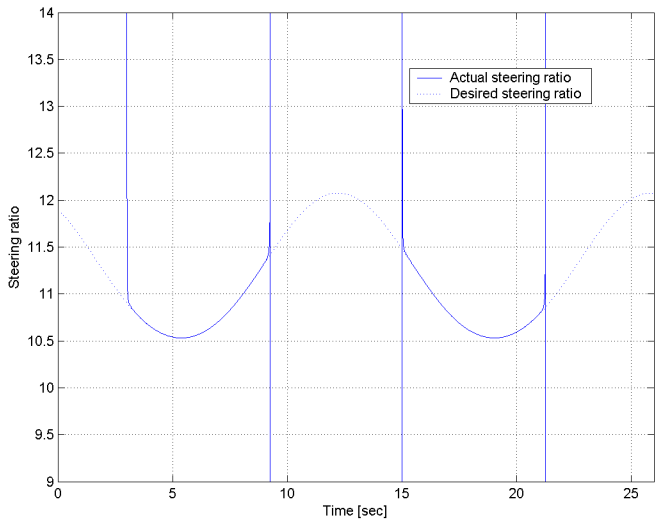

Figure 41: Desired and actual steering ratio for inner city scenario.

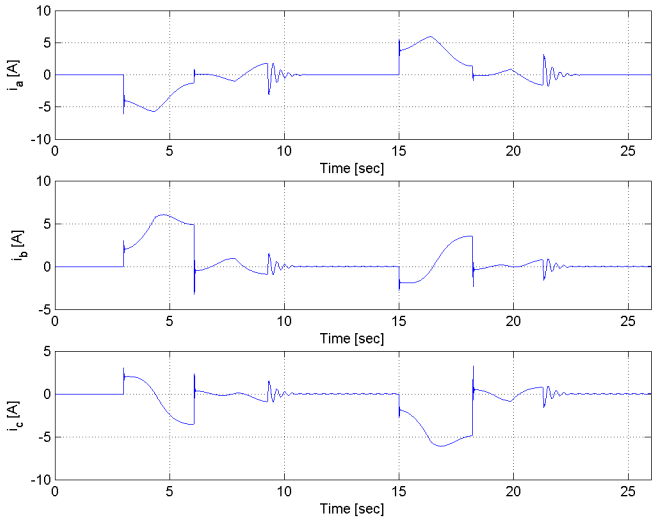

Figure 42: Phase currents for inner city scenario.

CHAPTER VII

DIGITAL POSITION CONTROLLER

In this chapter we move from the analog position controller presented in Chapter 4 to a digital position controller. This is because the position controller is to be implemented on a microcontroller. We first motivate direct digital design using state feedback. Subsequently we implement this type of controller and augment it with integral control and an estimator.

7.1 Motivation for Direct Digital Design

7.1.1 Direct and Indirect Digital Design

There are two approaches to designing a digital controller, i.e., direct and indirect design. The latter approach consists of developing a continuous controller first. Once a good continuous design is available, one strives to create a digital equivalent to the continuous controller that closely emulates the behavior of the continuous controller. That is why indirect design is also called emulation. The advantage of indirect design is that you do not have to design a whole new controller, but can effectively build on a previous continuous design. Emulation is still widely used today. The disadvantage of indirect design is that the sampling rate of the controller has to be considerably faster than the dynamics of the system. Even under this precondition indirect digital controller will generally involve a steady-state error.

In direct design on the other hand, we develop the controller in discrete time right away. Instead of taking the intermediate step of a continuous controller, one discretizes the plant and then develops the controller in discrete time. Unlike indirect design, direct design can also be applied if the controller is not much faster than the system. Moreover, the steady-state error can be brought to zero.

7.1.2 Application of Pole-Zero Mapping to Torque Controller

In the following we apply one indirect digital control method, namely pole-zero mapping, to our existing continuous outer controller. Our intention is to show that indirect design is

not a suitable approach to reach our performance objectives.

In pole-zero mapping all poles and zeros of the transfer function $G(s)$ of the continuous controller are mapped from the s- to the z-domain through

$$z = e^{sT} \tag{75}$$

where s is the original pole or zero, T the sampling period and z the new pole or zero.

In Subsection 4.3.2 we have developed a continuous torque controller using model matching with the transfer functions

$$C_1(s) = \frac{L(s)}{A(s)} \quad C_2(s) = \frac{M(s)}{A(s)} \tag{76}$$

By plugging in all the parameters we obtain the following poles, zeros and gains of $C_1(s)$ and $C_2(s)$ (Table 10). If we apply equation (75) to transform from the s- to the z-domain

	$C_1(s)$	$C_2(s)$
Poles		
s_{p1}	0	0
s_{p2}	-483.4055	-483.4055
Zeros		
s_{z1}	-200	$-75.0635 + j18.8616$
s_{z2}	-49.8462	$-75.0635 - j18.8616$
Gain		
k	1155.7207	1923.4235

Table 10: Poles, zeros and gains of $C_1(s)$ and $C_2(s)$.

we obtain Table 11. Hence the transfer functions of the discrete controller are

	$C_1(z)$	$C_2(z)$
Poles		
z_{p1}	1	1
z_{p2}	$e^{-483.4055T}$	$e^{-483.4055T}$
Zeros		
z_{z1}	e^{-200T}	$e^{(-75.0635+j18.8616)T}$
z_{z2}	$e^{-49.8462T}$	$e^{(-75.0635-j18.8616)T}$
Gain		
k	1155.7207	1923.4235

Table 11: Poles, zeros and gains of $C_1(z)$ and $C_2(z)$.

$$C_1(z) \quad = \quad 1155.7207 \frac{\left(z - e^{-200T}\right)\left(z - e^{-49.8462T}\right)}{(z-1)\left(z - e^{-483.4055T}\right)} \tag{77}$$

$$C_2(z) \quad = \quad 1923.4235 \frac{\left(z - e^{(-75.0635+j18.8616)T}\right)\left(z - e^{(-75.0635-j18.8616)T}\right)}{(z-1)\left(z - e^{-483.4055T}\right)}$$

Note that we have not fixed T yet. This allows simulating the discrete controller for different values of T thus determining the lowest feasible sampling rate.

7.1.3 Evaluation of Discrete Controller

We simulate the discrete outer controller for different values of T to find out the lowest feasible sampling rate or the highest period length respectively. We use the highway scenario for this. In Figure 43 we show the simulation results for the steering ratio for $T = 1$ msec,

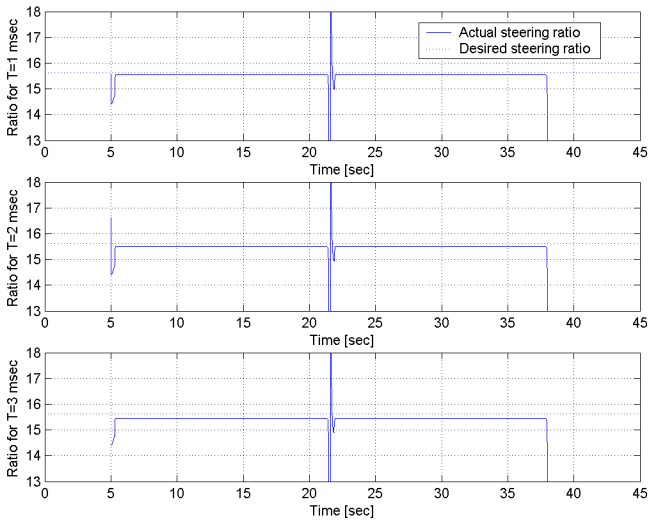

Figure 43: Desired and actual steering ratio for different values of T.

$T = 2$ msec and $T = 3$ msec. As one can see the steady-state error increases from 0.4% for $T = 1$ msec to 1.1% for $T = 3$ msec. If T is chosen to be larger than $T = 5$ msec, the system even becomes unstable. That is why with indirect design one would have to choose a sampling period around $T = 1$ msec. The CAN bus however only allows us to obtain measurements of the different system variables every 20 msec. Hence, we cannot supply the controller with up-to-date measurements at periods smaller than 20 msec. Moreover, since the number of operations per second increases linearly with the sampling rate, shorter sampling periods will result in more expensive microcontrollers. That is why we want the

controller to work at a sampling period which is a multiple of 20 msec. As we have just shown this cannot be achieved using a traditional indirect design approach. That is why we apply direct digital control.

7.2 Digital Feedforward Controller

One of the underlying reasons why we need a high sampling rate with the above approach is that the level of accuracy in the controller is relatively low. Both load torque and Coulomb friction are disturbances from the point of view of the controller. Hence, we had to use high gain integrators to quickly reject these disturbances.

We intend to change this approach in designing the digital controller. We increase the level of accuracy in the controller by incorporating a feedforward controller to reject load torque and Coulomb friction upfront. The remaining disturbance T_D torque is much smaller than in the case of the continuous controller. It is

$$T_D = T_{ff} - \frac{1}{G_H} T_L - \left(C_M + \frac{C_S}{G_H} \right) sgn \left(\frac{\mathrm{d}\delta_{sup}}{\mathrm{d}t} \right) \tag{78}$$

Since our intention is to make the disturbance torque T_D as small as possible, we have to make sure that the feedforward torque T_{ff} is close to the load torque and Coulomb friction. We therefore have to schedule T_{ff} as a function of the desired velocity of the superimposed steering angle $\dot{\delta}_{sup}$ determining Coulomb friction and the road-wheel angle δ_f determining load torque (Figure 44). We decide to use saturation functions for both

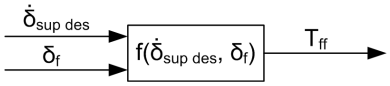

Figure 44: Calculation of T_{ff} from $\dot{\delta}_{sup}$ and δ_f.

Coulomb friction and load torque, because this type of function offers three advantages. First, a saturation function allows approximating the actual behavior of Coulomb friction and load torque quite well. Second, saturation functions are continuous. Third, saturation functions are relatively simple and therefore cheap to implement. We saturate the scheduled approximation of Coulomb friction at $C_M + C_S/G_H$ for $\dot{\delta}_{sup_{des}} = 1 * 10^{-4}$ s^{-1} and interpolate

linearly in between. Similarly, we saturate the scheduled approximation of load torque at 5 Nm/G_H for $\delta_f = 0.05775$ rad and interpolate linearly in between.

The graphical representation of T_{ff} as a function of $\dot{\delta}_{sup_{des}}$ and δ_f is shown in Figure 45.

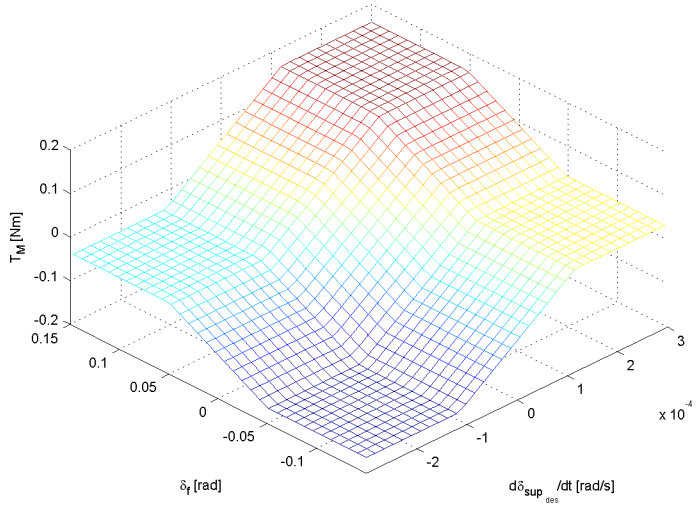

Figure 45: Visualization of feedforward control.

7.3 Digital Feedback Controller

In this section we develop a digital position controller for determining the torque command $T_{M_{des}}$. We do so in five steps. First, we derive the transfer function of the plant in the z-domain. Second, we motivate a state feedback approach rather than the model matching technique used in analog control. Third, we develop a general feedback compensator with performance similar to the one provided by the continuous controller developed in Section 4.2. Fourth, we introduce integral control by state augmentation to ensure zero steady-state error. Lastly, we set up an estimator to save cost on sensors.

7.3.1 Discretization of Plant

In order to apply a direct design approach, we first need to create a discretized model of the plant. In equation (78) we have introduced the feedforward torque T_{ff} to compensate

for load torque and frictional losses. With this, the original equation (17) of the mechanical submodule can be simplified to

$$(G_H J_M + J_{Load}) \frac{\mathrm{d}^2 \delta_{sup}}{\mathrm{d}t^2} = T_{fb} + T_D \tag{79}$$

Equation (79) in state-space form is

$$\underbrace{\begin{bmatrix} \dot{\delta}_{sup} \\ \ddot{\delta}_{sup} \end{bmatrix}}_{\dot{\mathbf{x}}} = \underbrace{\begin{bmatrix} 0 & 1 \\ 0 & 0 \end{bmatrix}}_{\mathbf{F}} \underbrace{\begin{bmatrix} \delta_{sup} \\ \dot{\delta}_{sup} \end{bmatrix}}_{\mathbf{x}} + \underbrace{\begin{bmatrix} 0 \\ \frac{1}{G_H J_M + J_{Load}} \end{bmatrix}}_{\mathbf{G}} T_{fb} + \underbrace{\begin{bmatrix} 0 \\ \frac{1}{G_H J_M + J_{Load}} \end{bmatrix}}_{\mathbf{G}} T_D \tag{80}$$

$$y = \underbrace{\begin{bmatrix} 1 & 0 \end{bmatrix}}_{\mathbf{H}} \underbrace{\begin{bmatrix} \delta_{sup} \\ \dot{\delta}_{sup} \end{bmatrix}}_{\mathbf{x}}$$

It is shown in [7] that the difference equation corresponding to equation (80) is

$$\begin{aligned} \mathbf{x}(k+1) &= \mathbf{\Phi}\mathbf{x}(k) + \mathbf{\Gamma} T_{fb}(k) + \mathbf{\Gamma} T_D(k) \\ y(k) &= \mathbf{H}\mathbf{x}(k) \end{aligned} \tag{81}$$

where

$$\begin{aligned} \mathbf{\Phi} &= \mathbf{I} + \mathbf{F}T + \frac{\mathbf{F}^2 T^2}{2!} + \frac{\mathbf{F}^3 T^3}{3!} + ... \\ \mathbf{\Gamma} &= \sum_{k=0}^{\infty} \frac{\mathbf{F}^k T^{k+1}}{(k+1)!} \mathbf{G} \end{aligned}$$

T is the sampling period. The z-transform of equation (81) is

$$\begin{aligned} [z\mathbf{I} - \mathbf{\Phi}]\, \mathbf{X}(z) &= \mathbf{\Gamma} T_{fb}(z) + \mathbf{\Gamma_1} T_D(z) \\ Y(z) &= \mathbf{H}\mathbf{X}(z) \end{aligned} \tag{82}$$

Hence, if we assume that the disturbance is zero, the transfer function is

$$\frac{Y(z)}{T_{fb}(z)} = \mathbf{H}\,[z\mathbf{I} - \mathbf{\Phi}]^{-1}\,\mathbf{\Gamma} \tag{83}$$

We now plug in the parameters from equation (80) and obtain

$$\begin{aligned} \mathbf{\Phi} &= \mathbf{I} + \mathbf{F}T + \frac{\mathbf{F}^2 T^2}{2!} + \frac{\mathbf{F}^3 T^3}{3!} + ... \\ &= \begin{bmatrix} 1 & 0 \\ 0 & 1 \end{bmatrix} + \begin{bmatrix} 0 & 1 \\ 0 & 1 \end{bmatrix} T = \begin{bmatrix} 1 & T \\ 0 & 1 \end{bmatrix} \end{aligned} \tag{84}$$

$$
\begin{aligned}
\mathbf{\Gamma} &= \sum_{k=0}^{\infty} \frac{\mathbf{F}^k T^{k+1}}{(k+1)!}\mathbf{G} \\
&= \left[\begin{bmatrix} T & 0 \\ 0 & T \end{bmatrix} + \begin{bmatrix} 0 & 1 \\ 0 & 0 \end{bmatrix} \frac{T^2}{2}\right] \begin{bmatrix} 0 \\ \frac{1}{G_H J_M + J_{Load}} \end{bmatrix} = \begin{bmatrix} \frac{T^2}{2(G_H J_M + J_{Load})} \\ \frac{T}{G_H J_M + J_{Load}} \end{bmatrix}
\end{aligned}
$$

Using (83) we get the discrete transfer function

$$
\begin{aligned}
\frac{Y(z)}{U(z)} &= G(z) = \begin{bmatrix} 1 & 0 \end{bmatrix} \left[z \begin{bmatrix} 1 & 0 \\ 0 & 1 \end{bmatrix} - \begin{bmatrix} 1 & T \\ 0 & 1 \end{bmatrix} \right]^{-1} \begin{bmatrix} \frac{T^2}{2(G_H J_M + J_{Load})} \\ \frac{T}{G_H J_M + J_{Load}} \end{bmatrix} \\
&= \frac{T^2}{2\left(G_H J_M + J_{Load}\right)} \frac{z+1}{(z-1)^2} = \frac{T^2}{2C} \frac{z+1}{(z-1)^2}
\end{aligned} \tag{85}
$$

7.3.2 Motivation for State Feedback Controller

Digital model matching would be the logical choice for the digital position controller. First, we used model matching for the analog position controller. Second, only the system output, i.e., δ_{sup} is needed for model matching. No additional measurements, e.g., of $\dot{\delta}_{sup}$ are necessary. This allows saving cost on sensors. Still, several challenges arise that cannot be overcome using model matching. In the following we describe these obstacles thus motivating the use of another control technique, i.e., state feedback.

The main obstacle in designing the model matching controller lies not so much in the derivation of the controller's transfer function, but rather in the prerequisite step, i.e., finding a suitable desired transfer function. The necessary and sufficient conditions to model matching according to [2] are

- #1 Pole-zero excess inequality: The relative degree of the desired transfer function has to be greater or equal to the relative degree of the plant transfer function.
- #2 Retainment of non-minimum-phase zeros: All zeros of the plant transfer function $G(z)$ on and outside the unit circle must be retained in $G_0(z)$.
- #3 Stability: All poles of $G_0(z)$ must lie inside the unit circle.

We need to fulfill these conditions while keeping with our control objective, i.e., tracking of a ramp reference input. In discrete time these requirements are fulfilled by a desired transfer function $G_d(z)$ with the following characteristics.

- #1 $G_d(1) = 1$
- #2 $\frac{\mathrm{d}}{\mathrm{d}z} G_d(1) = 0$

We first try using a desired transfer function of relative degree 1. Following the second condition to model matching mentioned above, we need to retain the non-minimum-phase zero at $z = -1$ in the desired plant transfer function. Hence $G_d(z)$ is

$$G_d(z) = \frac{z+1}{(z-p_1)(z-p_2)} \frac{(1-p_1)(1-p_2)}{2} \tag{86}$$

where p_1 and p_2 are the poles of the desired transfer function which we can choose. One can see immediately that $G_d(1) = 1$. The first condition of the control objective can therefore be fulfilled. We now check the second condition. The derivative of $G_d(z)$ at $z = 1$ is

$$\frac{\mathrm{d}}{\mathrm{d}z} G_d(1) = \frac{1}{2} - \frac{2 - p_1 - p_2}{(1-p_1)(1-p_2)} \tag{87}$$

which must be equal to zero. Hence, we have to ensure that

$$p_1 p_2 + p_1 + p_2 = 3 \tag{88}$$

In order for $G_d(z)$ to be an implementable transfer function p_1 and p_2 have to be either both real or conjugate complex. In the former case equation (88) cannot be fulfilled, because then either p_1 or p_2 or both would have to be ≥ 1, i.e., be on or outside of the unit circle. The resulting transfer function would be unstable. Equation (88) cannot be fulfilled in the latter case either. If there are two conjugate complex poles $p_{1/2} = a \pm jb$, then equation (88) becomes

$$a^2 + b^2 + 2a \quad = \quad 3 \tag{89}$$

In order for the transfer function to be implementable, the poles need to be inside the unit circle, i.e., $a^2 + b^2 < 1$ and $a, b < 0$. Equation (89) cannot be fulfilled while keeping with these conditions. As a result, digital model matching is not implementable with the given desired transfer function of relative degree 1.

In many instances problems of the above type can be resolved by choosing a greater degree of freedom, i.e., by moving from relative degree one to relative degree two. Then the

desired transfer function is

$$G_d(z) = \frac{z+1}{(z-p_1)(z-p_2)(z-p_3)} \frac{(1-p_1)(1-p_2)(1-p_3)}{2} \tag{90}$$

It is once again obvious that $G_d(1) = 1$ and the first condition can therefore be easily fulfilled. The derivative of $G_d(z)$ at $z = 1$ is

$$\frac{\mathrm{d}}{\mathrm{d}z} G_d(1) = \frac{1}{2} - \frac{3 - 2p_1 - 2p_2 - 2p_3 + p_1p_2 + p_2p_3 + p_1p_3}{(1-p_1)(1-p_2)(1-p_3)} \tag{91}$$

This should be equal to zero. As a result we know that

$$3p_1 + 3p_2 + 3p_3 - p_1p_2 - p_2p_3 - p_1p_3 - p_1p_2p_3 = 5 \tag{92}$$

Once again there are two possibilities for an implementable desired transfer function. There can either be three real poles inside the unit circle or there can be one real pole and two conjugate complex poles. We first look at the former case. In order to figure out if there is actually a solution to equation (92) inside the unit circle, we determine the potential extrema of the left hand side of this equation by taking the partial derivatives and setting them to zero. By doing so we obtain the potential extrema $(1, 1, 1)$ and $(-3, -3, -3)$. In order for the desired transfer function to be stable, the three poles must be $\left|p_{1/2/3}\right| < 1$ or in other words the poles must be inside of the cube shown in Figure 46. The two potential extrema are either on or outside the cube. Hence, there are no extrema inside of the cube representing the range of poles resulting in a stable desired transfer function. Since there are no maxima inside of the cube, the maximum value must be on the cube surface. One can show that the left hand side never becomes greater than five on the cube surface. That is why there is no solution to equation (92) inside of the cube. We can therefore conclude that there is no function of relative degree two with three real poles fulfilling the given requirements.

We now look at the second possibility of one real and two conjugate complex poles. In this instance the three poles are $p_1 = a + jb$, $p_2 = a - jb$ and $p_3 = c$. We plug this into equation (92) and obtain

$$6a + 3c - a^2 - b^2 - 2ac - a^2c - b^2c = 5 \tag{93}$$

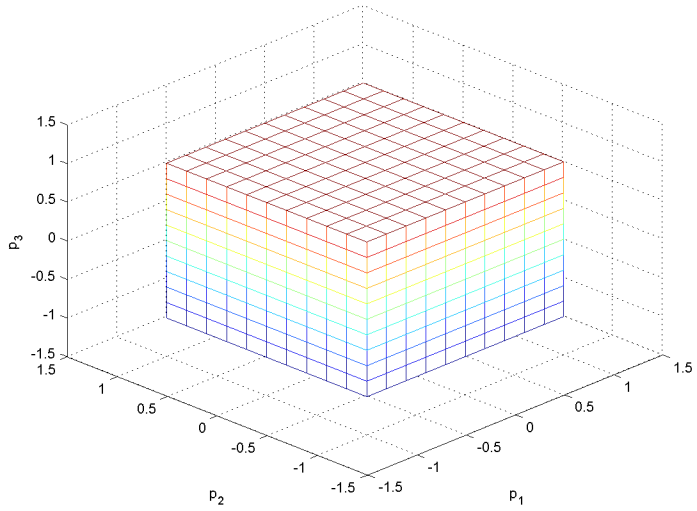

Figure 46: Feasible range of p_1, p_2 and p_3.

Once again we take the partial derivatives of the left side of equation (93) and determine the two potential extrema $(1, 0, 1)$ and $(-3, 0, -3)$. In order for the desired transfer function to be stable, we have to make sure that $\sqrt{a^2 + b^2} < 1$ and $|c| < 1$. Hence the feasible range of a, b and c is a cylinder (Figure 47). The two potential extrema are either on or outside the cylinder. Hence, there are no extrema inside of the cylinder representing the range of poles resulting in a stable desired transfer function. Since there are no maxima inside of the cylinder, the maximum value must be on the cylinder surface. One can show that on the cylinder surface, the left hand side never becomes greater than five. That is why there is no solution to equation (93) inside of the cylinder. We can therefore conclude that there is no function of relative degree two with one real pole and two conjugate complex poles fulfilling the given requirements.

Hence, we now know that there is neither a desired transfer function of degree one nor one of degree two fulfilling the given requirements. Digital model matching is therefore not implementable in these instances. We cannot make any definite assertion on whether model matching might be feasible for higher relative degrees. Based on the results for relative degrees one and two, we do however assert that there is a high probability that there will be no solution. Moreover, with the number of degrees increasing further, calculation will

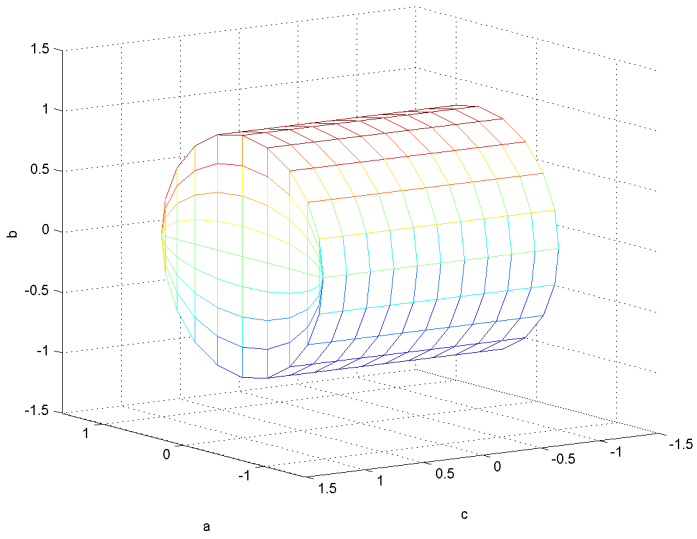

Figure 47: Feasible range of a, b and c.

become even more tedious than for relative degree two.

7.3.3 State Feedback Controller

As shown in the last subsection, ramp tracking is not achievable using model matching with desired transfer functions of relative degrees one and two. It can however be achieved using full-state feedback with a reference input. The underlying reason is that by feeding back both the angular position and angular velocity we can assign arbitrary root locations for these two states. The system is controllable. The controllability matrix is

$$\left[\Gamma \vdots \Phi\Gamma\right] = \begin{bmatrix} \frac{T^2}{2(G_H J_M + J_{Load})} & \frac{3T^2}{2(G_H J_M + J_{Load})} \\ \frac{T}{G_H J_M + J_{Load}} & \frac{T}{G_H J_M + J_{Load}} \end{bmatrix} \tag{94}$$

The matrix is nonsingular for our choices of T and vehicle parameters.

In order to control the two states of the system we implement the full-state feedback control structure with reference input as shown in Figure 48. In this figure **r** is the vector of

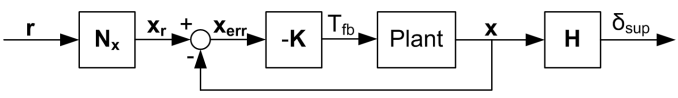

Figure 48: Structure of full-state feedback controller.

the reference inputs, i.e., $\delta_{sup_{des}}$ and $\dot{\delta}_{sup_{des}}$. We want to control both the angular position and the angular velocity and therefore $\mathbf{N_x} = \begin{bmatrix} 1 & 1 \end{bmatrix}^T$. $\mathbf{H}$ has already been given in equation (80). T_{fb} is the control output and is the difference between the reference state vector $\mathbf{x_r}$ and the actual state vector $\mathbf{x}$ times the negative vector of the feedback gain $\mathbf{K}$. The state equation in terms of the error vector

$$\mathbf{x_{err}} = \mathbf{x_r} - \mathbf{x} \tag{95}$$

is

$$\mathbf{x_{err}}(k+1) = \mathbf{\Phi x_{err}}(k) - \mathbf{\Gamma K x_{err}}(k) + \mathbf{\Gamma} T_D(k) \tag{96}$$

where Φ and Γ are identical to the symbols already used in equation (81).

As outlined above we want the digital controller to have performance similar to the previously developed continuous controller. That is why we intend to choose the two feedback coefficients in such a manner that we obtain an ITAE zero-velocity-error optimal system with $\omega_0 = 162$ sec^{-1}. With feedback of δ_{sup} and $\dot{\delta}_{sup}$, we obtain a characteristic equation of degree two in the s-domain, which is

$$s^2 + 3.2\omega_0 s + {\omega_0}^2 \tag{97}$$

The two roots of equation (97) are

$$s_{1/2} = \left(-1.6 \pm \sqrt{1.56}\right)\omega_0 \tag{98}$$

We transform the roots into the z-domain

$$z_{1/2} = e^{s_{1/2}T} = e^{\left(-1.6 \pm \sqrt{1.56}\right)\omega_0 T} \tag{99}$$

Hence, the characteristic equation in the z-domain is

$$z^2 - \left(e^{\left(-1.6+\sqrt{1.56}\right)\omega_0 T} + e^{\left(-1.6-\sqrt{1.56}\right)\omega_0 T}\right) z + e^{-3.2\omega_0 T} = 0 \tag{100}$$

The characteristic equation of the system with control is

$$\begin{aligned} \det\left|z\mathbf{I} - \mathbf{\Phi} + \mathbf{\Gamma K}\right| &= 0 \qquad (101) \\ \det\left|z\begin{bmatrix} 1 & 0 \\ 0 & 1 \end{bmatrix} - \begin{bmatrix} 1 & T \\ 0 & 1 \end{bmatrix} + \begin{bmatrix} \frac{T^2}{2(G_H J_M + J_{Load})} \\ \frac{T}{G_H J_M + J_{Load}} \end{bmatrix} \begin{bmatrix} K_1 & K_2 \end{bmatrix}\right| &= 0 \end{aligned}$$

Equations (100) and (101) have to be identical. Hence, we have to choose

$$\begin{aligned} K_1 &= \frac{G_H J_M + J_{Load}}{T^2}\left(e^{-3.2\omega_0 T} - e^{-0.351\omega_0 T} - e^{-2.849\omega_0 T} + 1\right) \\ K_2 &= \frac{G_H J_M + J_{Load}}{2T}\left(-e^{-3.2\omega_0 T} - e^{-0.351\omega_0 T} - e^{2.849\omega_0 T} + 3\right) \end{aligned} \tag{102}$$

If we plug in all the parameters, we obtain the actual numerical values of $\mathbf{K}$

$$\begin{aligned} K_1 &= 38.2322 \\ K_2 &= 3.5191 \end{aligned} \tag{103}$$

7.3.4 Integral Control by State Augmentation

The underlying assumption behind the digital controller derived in the previous subsection is that we do not have any disturbance torque T_D. This will generally not be the case. Hence, any non-vanishing disturbance will result in a steady-state error. We do not want this. That is why we augment the model of the plant with an integrative state. The integrative state x_{IS} is given by

$$x_{IS}(k+1) = x_{IS}(k) + y(k) = x_{IS}(k) + \mathbf{H}\mathbf{x_{err}}(k) \tag{104}$$

The augmented plant model is therefore

$$\begin{bmatrix} x_{IS}(k+1) \\ \mathbf{x_{err}}(k+1) \end{bmatrix} = \begin{bmatrix} 1 & \mathbf{H} \\ 0 & \mathbf{\Phi} \end{bmatrix} \begin{bmatrix} x_{IS}(k) \\ \mathbf{x_{err}}(k) \end{bmatrix} + \begin{bmatrix} 0 \\ \mathbf{\Gamma} \end{bmatrix} T_{fb}(k) + \begin{bmatrix} 0 \\ \mathbf{\Gamma} \end{bmatrix} T_D(k) \tag{105}$$

The control law is also augmented and becomes

$$T_{fb}(k) = -\begin{bmatrix} K_{IS} & \mathbf{K} \end{bmatrix} \begin{bmatrix} x_{IS}(k) \\ \mathbf{x_{err}}(k) \end{bmatrix} \tag{106}$$

Once again we want the digital controller to perform like the continuous controller developed in Chapter 4. However, unlike the continuous controller, we now have improved the level of accuracy of the controller by compensating the load torque T_L and Coulomb friction using the feedforward controller. That is why it is not necessary to have a disturbance rejection as fast as in the continuous controller where we chose a pole at $s = -\alpha = -200$. Moreover, high-gain feedback of the integrative state will result in higher overshoot and more control effort. We choose $K_{IS} = 0.1$ which allows rejecting 60 % of a step disturbance within around 4 sec. The actual performance however also depends on the sampling period T.

7.3.5 Reduced-Order Estimator

We want to calculate the velocity of the superimposed steering angle $\dot{\delta}_{sup}$ using a reduced-order estimator rather than measuring it using sensors. The reason behind this is that you need very precise and costly sensors if you want to measure $\dot{\delta}_{sup}$, because you have to differentiate the original signal δ_{sup}. We intend to save cost by finding a way around this.

We assume that δ_{sup} is measurable whereas $\dot{\delta}_{sup}$ is not. Hence, the digital system description is

$$\begin{aligned}
\begin{bmatrix} \delta_{sup}(k+1) \\ \dot{\delta}_{sup}(k+1) \end{bmatrix} &= \begin{bmatrix} 1 & T \\ 0 & 1 \end{bmatrix} \begin{bmatrix} \delta_{sup}(k) \\ \dot{\delta}_{sup}(k) \end{bmatrix} \\
&\quad + \begin{bmatrix} \frac{T^2}{2(G_H J_M + J_{Load})} \\ \frac{T}{G_H J_M + J_{Load}} \end{bmatrix} T_{fb}(k) + \begin{bmatrix} \frac{T^2}{2(G_H J_M + J_{Load})} \\ \frac{T}{G_H J_M + J_{Load}} \end{bmatrix} T_D(k) \\
y(k) &= \begin{bmatrix} 1 & 0 \end{bmatrix} \begin{bmatrix} \delta_{sup}(k) \\ \dot{\delta}_{sup}(k) \end{bmatrix}
\end{aligned} \tag{107}$$

To simplify the notation we neglect the disturbance torque T_D in the derivation of the estimator. The dynamics of the unmeasured state $\dot{\delta}_{sup}(k)$ are

$$\dot{\delta}_{sup}(k+1) = \dot{\delta}_{sup}(k) + \frac{T}{G_H J_M + J_{Load}} T_{fb}(k) \tag{108}$$

We use equation (108) to calculate the estimated state $\hat{\dot{\delta}}_{sup}$. The dynamics of the measured state are given by

$$\underbrace{\delta_{sup}(k+1) - \delta_{sup}(k) - \frac{T^2}{2\left(G_H J_M + J_{Load}\right)} T_{fb}(k)}_{\text{known}} = T\dot{\delta}_{sup}(k) \tag{109}$$

Note that equation (109) represents a relationship between the unknown state and known quantities. We use this to feed back the difference between the left hand side of equation (109) and $T\hat{\dot{\delta}}_{sup}$ calculated in the estimator, i.e.,

$$\begin{aligned}
\hat{\dot{\delta}}_{sup}(k+1) &= \hat{\dot{\delta}}_{sup}(k) + \frac{T}{G_H J_M + J_{Load}} T_{fb}(k) \\
&\quad + L_r \left[\delta_{sup}(k+1) - \delta_{sup}(k) - \frac{T^2}{2\left(G_H J_M + J_{Load}\right)} T_{fb}(k) - T\hat{\dot{\delta}}_{sup}(k) \right]
\end{aligned} \tag{110}$$

The equation of the estimate error $\tilde{\dot{\delta}}_{sup}$ obtained by subtracting (110) from (108) is

$$\tilde{\dot{\delta}}_{sup}(k+1) = [1 - L_r T]\, \tilde{\dot{\delta}}_{sup}(k) \tag{111}$$

We now choose L_r such that the root of the characteristic equation

$$z - 1 + L_r T = 0 \tag{112}$$

corresponds to our desired root location. In determining the desired roots one has to make a tradeoff between the swiftness of disturbance rejection and the stability of the system. Due to unmodeled disturbances and sensor errors, excessively fast disturbance rejection can destabilize the system. We choose the desired root location $z = 0.6$. According to [7] this corresponds to a settling time of 0.4 sec within a 1 % tolerance band. With that we know

$$L_r = \frac{1 - 0.6}{T} = 6.6667 \tag{113}$$

By plugging all the parameters into equation (110) we obtain the final reduced-order estimator equation given by

$$\hat{\dot{\delta}}_{sup}(k+1) = 0.6\hat{\dot{\delta}}_{sup}(k) + 0.8856 T_{fb}(k) + 26.6667\, [\delta_{sup}(k+1) - \delta_{sup}(k)] \tag{114}$$

In Subsection 7.2 we required measurements of the velocity of the superimposed steering angle $\dot{\delta}_{sup}$ to cancel nonlinear terms. That is why we also feed the current controller with the results of the estimator. That way we do not need measurements of $\dot{\delta}_{sup}$ anywhere in the system.

7.4 Evaluation of Digital Position Controller with Final Model

The scenarios used here are the same as in Chapters 4 and 6. The steering input, the velocity profile and all other parameters are also identical.

7.4.1 Scenario 1: Highway

We do not give the results for the torque output and the phase currents here as these are largely identical to those already described in Chapters 4 and 6. The focus here is on how

far performance degrades due to the digital nature of the controller using an estimator and operating at a sampling period of 20 msec. We first take a look at the actual steering ratio as compared to the desired steering ratio in the highway scenario (Figure 49). Unlike the

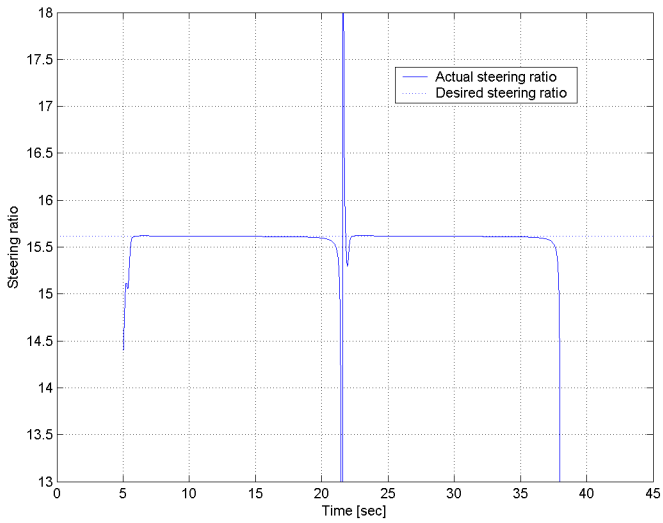

Figure 49: Desired and actual steering ratio for highway scenario.

previous simulations with the analog position controller we now have overshoot in terms of the steering ratio at around five seconds. Moreover, it takes longer for the system to reach the desired steering ratio of 15.61. Although there is some degradation of performance, the overall results are still satisfactory. This can also be seen if one looks at the actual superimposed steering angle δ_{sup} as compared to the desired superimposed steering angle δ_{sup_d} in Figure 50. As one can see the two angles are so close to each other that the two curves run on top of each other in the diagram.

7.4.2 Scenario 2: Inner City

Once again we look at the actual steering ratio compared to the desired steering ratio (Figure 51). Now there is a noticeable discrepancy between the curve for the desired steering ratio and the curve for the actual steering ratio. Considerable discrepancies occur around 8 sec, 16 sec and 20 sec. The primary reason for the degradation in performance is the use of the estimator rather rather than a sophisticated sensor. This effect is discussed in more detail

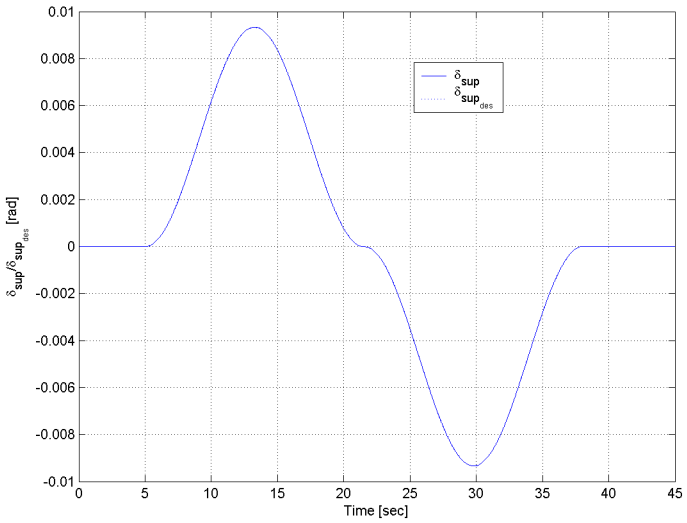

Figure 50: Desired and actual superimposed steering angle for highway scenario.

in Subsection 8.5. The point is however that although discrepancies are now noticeable, the overall performance of the controller is still satisfactory. One of the reasons for this is that all of the above mentioned periods where noticeable discrepancies occur are at instances where the superimposed steering angle δ_{sup} is close to zero. Due to the definition of the steering ratio as the quotient of δ_{SW} and δ_{sup}, small differences between the desired superimposed steering angle δ_{sup_d} can result in large errors in terms of the steering ratio. This is however no limitation to the performance of the system, because at small steering angles even large variations in the steering ratio cannot be noticed by the driver. We underline this using Figure 52. In this figure we show the desired superimposed steering angle δ_{sup_d} as compared to the actual superimposed steering angle δ_{sup}. As one can see the curves for δ_{sup_d} and δ_{sup} overlap to such an extent that they can barely be distinguished from each other. Since δ_{sup} is what is ultimately noticed by the driver, performance is sufficient.

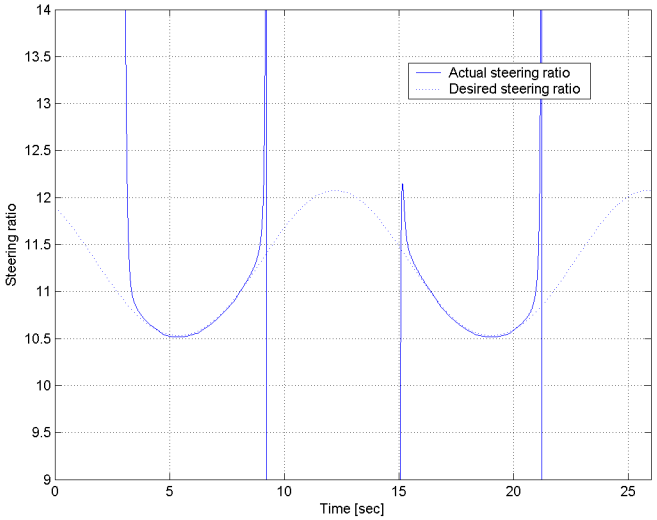

Figure 51: Desired and actual steering ratio for inner city scenario.

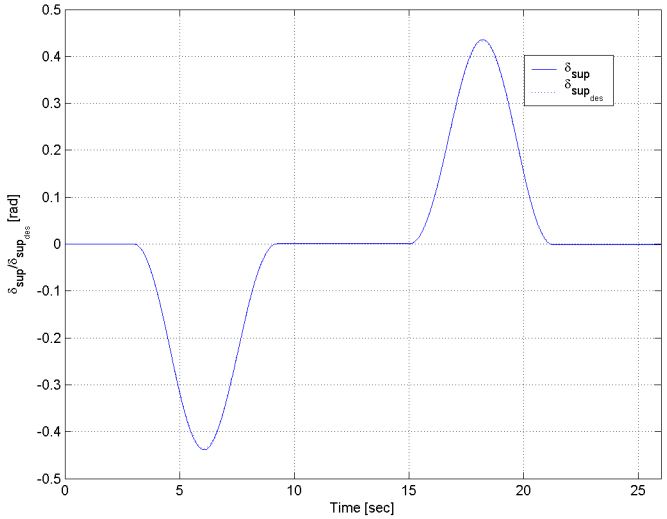

Figure 52: Desired and actual superimposed steering angle for inner city scenario.

CHAPTER VIII

VALIDATION

In this last chapter we validate our design. In doing so we apply the Validation Square. This is a method to validate design methods and research that has been developed at the System Realization Laboratory at the Georgia Institute of Technology. An extensive introduction into the underlying philosophy of the Validation Square is given in [19]. In this chapter we first introduce the Validation Square and the four principal steps that it comprises. We then take the work presented as part of this thesis through these four steps thus establishing confidence in the validity of our work.

8.1 Introduction to the Validation Square

The outstanding strength of the Validation Square is that it offers designers a framework to address both the quantifiable and the non-quantifiable or open aspects of design. The principal idea behind it is that establishing the validity of a design is a process in which one gradually builds confidence in the proposed solution. In the validation process one needs to analyze both the actual results and the approach that was taken to come up with the design. This is accounted for by breaking the Validation Square up into four quadrants. In each of the four quadrants one specific aspect of validation is carried out. The four quadrants are shown in Figure 53. In the first quadrant one assesses the theoretical structural validity. This is the internal consistency of the design both in terms of its structure and its derivation. In the quadrant for empirical structural validity one needs to show that the example problems used to validate the design are indeed appropriate to test specific aspects. In the third quadrant one assesses the empirical performance validity. One looks at the results of the example problems outlined in the second quadrant to establish confidence in the design for the given example problems. In the last quadrant one needs to reflect on the validity of the design beyond the example problems discussed in quadrants two and three. Since

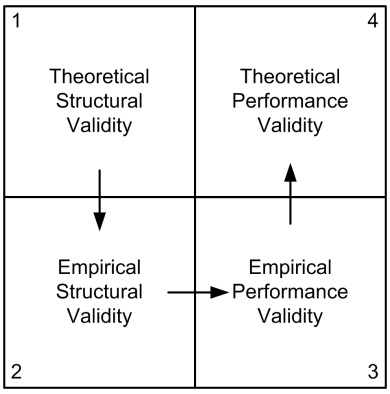

Figure 53: Validation Square.

in most instances it is not possible to actually prove the validity outside of the example problems, this step requires a leap of faith. The leap of faith must be based on a prior process of building confidence in the design.

In the following we take our design of the superimposed steering system through all four quadrants. We particularize each step to this specific example.

8.2 Theoretical Structural Validity

As outlined above we need to show that the design is internally consistent both in terms of its derivation and the actual controller. That is why theoretical structural validity breaks down into two main parts.

- Internal consistency of derivation: One needs to raise the question if the design approach has the structure that can be expected to lead to a valid design solution. The emphasis here is on the process.

- Internal consistency of results: One needs to determine if the model and control techniques that the design is built on can be expected to be valid from a scientific perspective. Moreover, one has to assess if the structure of the controller is logical in the sense that the functions of the different parts of the controller are well-defined. The emphasis here is on the result.

8.2.1 Internal Consistency of Derivation

In designing the system we have aimed at three things. First, we tried to implement a clear structure. Second, we intended to approach the solution from the general to the specific. Third, we checked and evaluated our results at several instances in the design process. These concepts have been illustrated in Figure 54. Except for Chapter 1 and Chapter 8, which

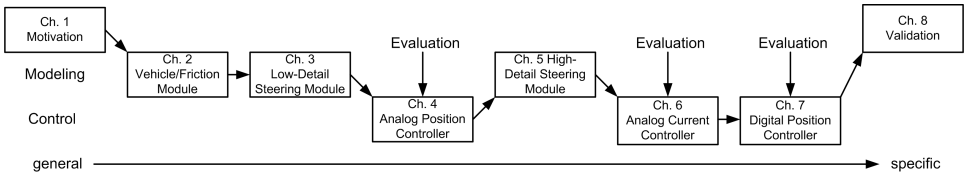

Figure 54: Internal consistency of derivation.

have introductory or closing character respectively, we have divided all chapters into either modeling or control chapters. The underlying philosophy behind this is that modeling and control are entirely different things and should be treated as such. Keeping these two things separated also facilitates the latter use of the controller and the model as separate entities. Thus the model and the controller can be used independently.

We also proceed from the general to the specific. In Chapter 1 we start by underlining the usefulness of a superimposed steering system from a comfort and safety perspective. In Chapter 2 we then set up the model of the vehicle dynamics. This model is still relatively general in that it can be used for many modeling and control applications in vehicle dynamics. In Chapter 3 we narrow down from this more general class of tasks to those tasks involving control inputs in the steering system. The first evaluation of these preliminary results takes place in Chapter 4 by designing and simulating a position controller to be used in this model. We set up two scenarios for this which can be considered typical driving situations. In Chapter 5 we narrow down the task even further by focusing on superimposed steering systems with permanent-magnet synchronous motors. In Chapter 6 the controller is also brought to this level of detail by incorporating current control. Moreover, the second evaluation takes place at this stage. We assess the results by comparing them to those from the previous simpler model and controller. Finally, in Chapter 7 we move from analog to

digital position control. In doing so we make use of the knowledge obtained throughout the previous chapters. Simulation results are evaluated once again.

Based on these observations we claim that our design approach has a clear structure, proceeds from the general to the specific and included evaluations at multiple instances. We therefore conclude that the derivation of results was internally consistent.

8.2.2 Internal Consistency of Results

The results of our work come in the form of a model and a controller. In the model we have tried to ensure consistency by structuring the model like the real vehicle. There are three main parts to the real vehicle. The vehicle body, the steering module and the tire-road interface. We mapped these into three distinct modules, namely the vehicle module, the steering module and the friction module (Figure 55). By embracing the concept of

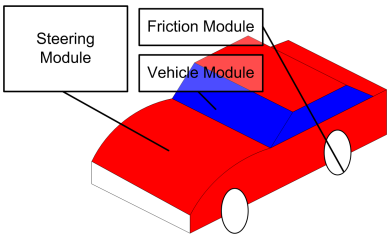

Figure 55: Model Structure.

modularity we could ensure that the interaction between different modules is clearly defined. Each module has inputs and outputs through which it interacts with the other modules.

The controller has also been structured. We divided the overall controller into two cascaded loops. This is a concept that can be found in several textbooks, notably [16]. In the outer loop we control the angular position δ_{sup} and in the inner loop we control the currents i_q and i_d.

In implementing the model and the controller we used several concepts. In order to build up confidence in that these are consistent, we now list the concepts and describe their origin.

- Single-track model: The model of the vehicle dynamics is based on the single-track or bicycle model. This is a very old and well-established model for vehicle dynamics.

It was first published in [20] in 1940. It is however still widely used today, notably in papers on active steering ([8], [14], [18]) which are very close to what has been done here.

- qd motor model: We have modeled the dynamics of the motor in the qd frame of reference by applying Park's transformation. This is a common approach in motor control and is used among others in [12] and [13].

- Digital state feedback control: In order to control position we used digital state feedback control based on direct digital design. A very similar approach has been taken in [7].

- Feedback linaerization: We used feedback linearization for the current controllers. This approach was based on the introduction to feedback linearization in [11].

Based on the above observations we conclude that the work is based on consistent concepts in the literature that were used in an organized manner to come to well-structured results. The conclusion is therefore that the controller has theoretical structural validity.

8.3 Empirical Structural Validity

We now need to show that the example problems that we use in the third quadrant of the Validation Square are appropriate to test specific aspects. In a control context we have to test the two principal activities of any control task. On the one hand, one has to lay down the control structure, i.e., the type of controller. On the other hand, the numerical values of the control parameters for the given type must be determined. We intend to show that the controller is valid in both these aspects by introducing two different test scenarios.

- Validity of control structure: We intend to demonstrate that the structure of the controller is appropriate by showing that suitable results can be obtained for a wide range of control parameters and not only for the specific set given in the previous chapters. The underlying assumption is that satisfying control performance over a wide range of control parameters indicates a suitable control structure.

- Validity of control parameters: We plan to show that the choice of control parameters was right by demonstrating that control performance remains appropriate despite changes in the plant. Hence, the underlying assumption is that robustness is an indication that the control parameters have been chosen appropriately.

8.4 Empirical Performance Validity

In the last section we have pointed out what we intend to show in going through two examples. In this third quadrant of the Validation Square we now actually set up and go through the examples thus establishing confidence in the control structure as well as control parameters. In order to assess performance we need a performance metric. This is what we introduce performance indices for.

8.4.1 Control Performance Indices

In this subsection we set up indices for measuring control performance and control effort. Control performance can be characterized by

$$x_{err} = x_d - x \tag{115}$$

This is the difference between the actual output x of the controlled parameters and what you initially went out to achieve, which is x_d.

If the performance is evaluated at multiple points in time, then one either has to calculate the average value or integrate over the error and divide by the length of the integral. Moreover, in considering x_{err} at multiple points in time one has to consider either the absolute value or x_{err} to an even power so that positive and negative values of x_{err} cannot cancel each other. Using x_{err} squared has the additional effect of punishing large errors disproportionately compared to smaller errors. This constitutes a reasonable assumption in many systems, notably in the case of the superimposed steering system. Hence we define control performance as

$$CP = \frac{1}{T}\int_0^T (x_d(t) - x(t))^2 \, \mathrm{d}t = \frac{1}{T}\int_0^T x_{err}(t)^2 \, \mathrm{d}t \tag{116}$$

In order to completely determine the control performance index for the example of the superimposed steering system, we still have to decide on one specific parameter in terms of which we determine performance. There are two possibilities here. We can either define performance in terms of the steering ratio or we can define it in terms of the superimposed steering angle δ_{sup}. The latter choice is more logical, because the steering ratio is not always defined. As we already mentioned in Subsection 4.4.1 the steering ratio is not defined if δ_{sup} is equal to zero. That is why the control performance index for the superimposed steering system is

$$CP = \frac{1}{T} \int_0^T \left(\delta_{sup_{des}}(t) - \delta_{sup}(t)\right)^2 \, \mathrm{d}t \tag{117}$$

We now take a similar approach to come up with a performance index for control effort. There are many ways in which control effort can be defined. One might for instance consider the torque output of the electric motor. In doing so one would however not consider the electrical dynamics of the motor and the resulting losses. We consider the total power consumption of the superimposed steering system to be the most logical choice for describing the control effort.

In Chapter 5 we transformed the motor dynamics into the qd frame of reference. That is why we also describe power consumption in the qd frame of reference. Power is defined by the product of voltage and current. We integrate power over time and divide by the integral length. Finally, we sum up the results for the q- and the d-axis. This gives us the control effort index

$$CE = \frac{1}{T} \int_0^T |v_q(t) i_q(t)| \, \mathrm{d}t + \frac{1}{T} \int_0^T |v_d(t) i_d(t)| \, \mathrm{d}t \tag{118}$$

8.4.2 Validity of Control Structure

As outlined in the section on empirical structural validity, we need to show that we have a valid control structure. The way to show this is by varying the control parameters and showing that performance remains acceptable. It is however not feasible to vary all six control parameters independently of each other. The resulting problem would simply be too large. The objective therefore consists of exploring the design space with as few parameters

as possible. This is a very active area of research in the field of design. Numerous methods have been suggested to do so, notably the Robust Concept Exploration Method (RCEM) suggested in [3]. Using this method one can explore the design space in a mathematical manner. What we take over from this method is the concept of response surfaces and the idea that most designs have dominant and weak design parameters. The weak design parameters have either little effect on the overall performance of the proposed solution or are highly dependent on the dominant design factors and can therefore be calculated from those.

The dominant parameters in the superimposed steering system are the sampling period T of the digital position controller and its natural frequency ω_0. In exploring the design space we consider these to be independent parameters. All other parameters, i.e., the weak or dependent parameters are changed as a function of the dominant parameters. In total there are two independent and four dependent control parameters. These are shown in Table 12 according to the part of the controller in which they occur, i.e., digital position controller, reduced-order estimator and analog current controller. We evaluate the performance indices

Digital position controller		
T	sampling period	independent
ω_0	natural frequency	independent
K_{IS}	integral state gain	dependent
Reduced-order estimator		
L_r	estimator feedback gain	dependent
Current controller		
K_I	current integral gain	dependent
K_P	current proportional gain	dependent

Table 12: Independent and dependent control parameters.

for different values of T and ω_0. Before we can do so, we need to establish functions for the four dependent parameters allowing us to map from a combination of T and ω_0 to the actual values of the dependent parameters. It is essential to choose the four dependent parameters in such a manner that all parameters taken together constitute a sensible combination for the overall controller. We base the derivation of the four functions for the dependent parameters on two premises.

- # 1 Results from previous chapters as a subset: If we choose the sampling rate and the natural frequency like in the previous chapters, i.e., $T = 60$ msec and $\omega_0 = 162$ sec^{-1} then the functions should give us the same values for the dependent parameters as those we already used in the previous chapters. As a result the design from the previous chapters is a subset of the design variations presented in this chapter.

- #2 Maintain principal characteristics: Each function is selected such that an important characteristic of the controller is maintained across all combinations of T and ω_0. There are four characteristics listed in Table 13. Each of these characteristics affects one dependent parameter.

Dependent parameter	Characteristic
K_{IS}	integral gain K_{IS} proportional to position error gain K_1
L_r	estimator root at $z = -0.6$
K_I	natural frequency of current controller ω_1 proportional to ω_0
K_P	current controller has damping ratio of $\zeta = 9.761$

Table 13: Principal characteristics to be maintained.

We now develop the functions from the two premises. We first look at K_{IS}. We assume that the ideal choice of K_{IS} is to change K_{IS} linearly with K_1, i.e., $K_{IS} = kK_1$ with k chosen such that the first premise is satisfied. In this instance $k = 2.6156 * 10^{-3}$. K_1 on the other hand depends on T and ω_0 as we have already shown in equation (102), i.e.,

$$K_1 = \frac{G_H J_M + J_{Load}}{T^2}\left(e^{-3.2\omega_0 T} - e^{-0.351\omega_0 T} - e^{-2.849\omega_0 T} + 1\right) \tag{119}$$

With that we can calculate K_{IS}. We now look at the estimator feedback gain L_r. We want to maintain the root of the estimator at $z = 0.6$. From equation (112) we can therefore conclude that L_r needs to be

$$L_r = \frac{1 - 0.6}{T} \tag{120}$$

We now get to the two parameters of the current controller. First, we look at the current integral gain K_I. The requirement consists of maintaining a proportional relationship between ω_0 and ω_1, i.e., $\omega_1 = k\omega_0$ with k chosen such that the first premise is satisfied. In this case $k = 2.4691$. With that K_I should be

$$K_I = L' (k\omega_0)^2 \tag{121}$$

Finally, we have to determine K_P. We choose K_P to maintain the damping ratio at $\zeta = 9.761$. From equation (74) we know that

$$\frac{R + K_P}{L'} = 2\zeta\omega_1 \tag{122}$$

From this we can conlude that

$$K_P = 2 * \zeta * 2.4691\omega_0 L' - R \tag{123}$$

We have expressed all dependent parameters as functions of the independent parameters and system constants. This can be summarized by

$$\begin{aligned} K_{IS}(T, \omega_0) &= 2.6156 * 10^{-3} \frac{G_H J_M + J_{Load}}{T^2} \left(e^{-3.2\omega_0 T} - e^{-0.351\omega_0 T} - e^{-2.849\omega_0 T} + 1 \right) \\ L_r(T) &= \frac{0.4}{T} \\ K_I(\omega_0) &= 6.0966 L' {\omega_0}^2 \\ K_P(\omega_0) &= 48.2018 L' \omega_0 - R \end{aligned} \tag{124}$$

We have determined independent parameters and dependent parameters. We now use these results to obtain knowledge of how the two independent control parameters affect control performance and control effort. In doing so we use the concept of the response surface. A response surface is a graphical representation of a performance criterion such as the control performance index CP and the control effort index CE over the independent control parameters. We use the inner city scenario, because this scenario requires higher performance.

We evaluate the control performance index CP by setting the sampling period T to multiples of 20 msec, which is the sampling rate of the CAN bus. We also vary the natural frequency ω_0 at intervals of 40 sec^{-1}. The original choice of parameters that we used in the previous chapters, i.e., $\omega = 162$ sec^{-1} and $T = 60$ msec, is now located in the center of the response surface. The results are shown in Figure 56. On the one hand, these results confirm what one would logically expect, i.e., lower sampling periods and higher natural frequencies result in better performance. On the other hand, we can conclude from the response surface on the importance of the individual parameters in determining the control performance.

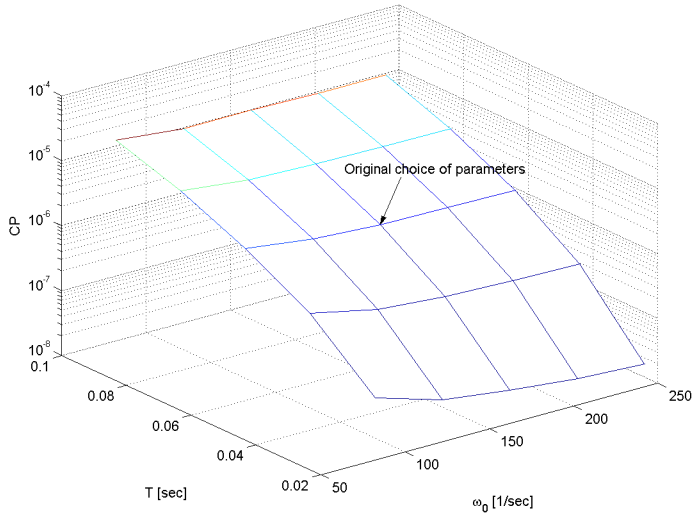

Figure 56: CP response surface for changes in control parameters.

- Changes in T: Changes in the sampling period T have a strong effect on the control performance index CP. As we reduce the sampling period from 100 msec to 20 msec, CP decreases to about one percent of its original value. The choice of the sampling period is the single most important decision in adjusting the performance of the controller.

- Changes in ω_0: Compared to the effect of changes in T, variations in ω_0 are negligible. Increasing the natural frequency by a factor of five cuts the control performance index by approximately one half across all choices of T. Hence, ω_0 is not that crucial in determining the performance of the system.

We now look at the response surface for the control effort index CE for exactly the same range of T and ω_0 (Figure 57). We analyze the results.

- Negligible variations in CE: The mean of CE for the given range of T and ω_0 is 0.0360 W and the standard deviation is merely 0.8148 mW. Hence, the variations in CE are very small. In fact variations are so small that all solutions can be considered approximately equivalent in terms of control effort.

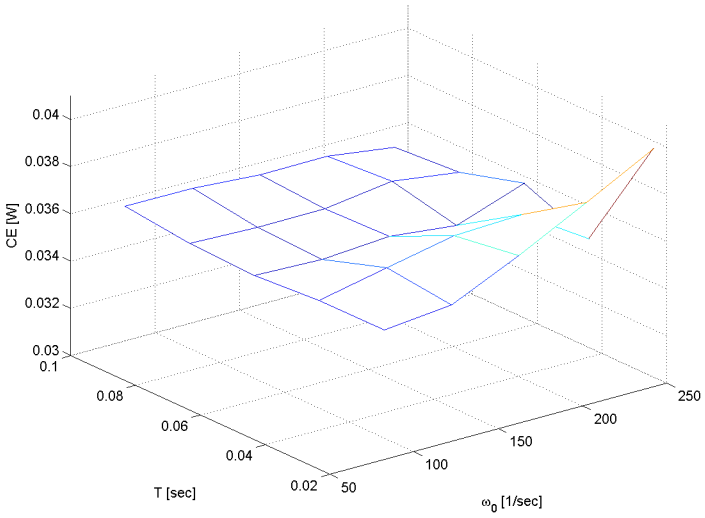

Figure 57: CE response surface for changes in control parameters.

Looking at the response surfaces for the control performance and control effort we observe that changes in control parameters affect the system in the way that we would expect. This indicates that the control structure has been understood and can be used over a wide range of control parameters. We conclude that the control structure is valid.

8.4.3 Validity of Control Parameters

In the last subsection we have assessed the validity of the control structure by changing the control parameters for an unchanging control structure. We now assess the validity of the control parameters by observing how the performance indices change for variations in the plant model and disturbances. In other words we assess the robustness of the controller.

In order to do so we once again use the concept of response surfaces. We modify two parameters. We vary the load torque in the plant by $\pm\,60\%$. This corresponds to modeling errors. We also introduce measurement errors in the sensor for δ_{sup} that feeds the controller. The sensor has a constant offset from the actual value. This corresponds to effects not considered in the controller. The details of this scenario are given in Table 14.

We now look at the response surface for the control performance index CP (Figure 58). The original choice of plant parameters that were used to calculate the controller is

Modeling errors	
modified load torque	$T_{L_{new}} = k * T_L$ with $k \in \{0.4, 0, 6, 1, 1.4, 1.6\}$
Unmodeled effects	
imprecise position sensor	$\delta_{sup_{Sensor}} = \delta_{sup} + e$ with $e \in \{\pm 10^{-4}, \pm 2 * 10^{-4}\}$

Table 14: Modifications to assess validity of control parameters.

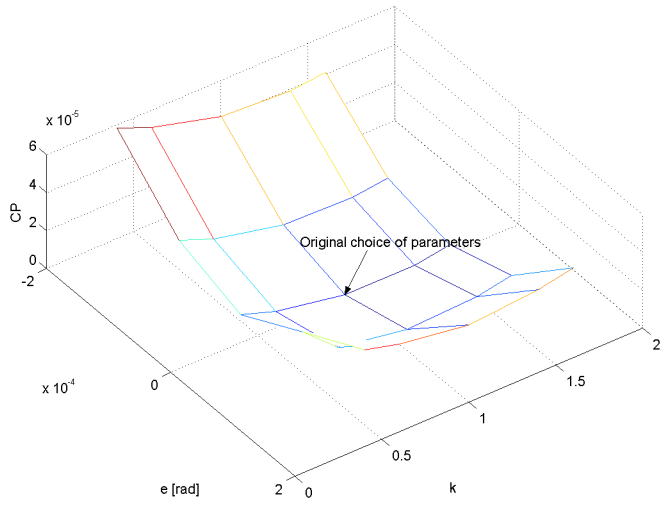

Figure 58: CP response surface for changes in plant parameters.

located in the center of the surface. At this point CP is the lowest, i.e., we have the highest performance. If we move away from that point by changing the load torque or introducing a measurement error, the performance deteriorates. It has however been verified by also looking at the time response of the steering ratio that the performance within the range of plant parameters shown in Figure 58 is satisfying. We can therefore conclude that control performance is robust for the given scenario in view of changes in the load torque of up to 60 % and measurement errors in δ_{sup} of up to $\pm 10^{-4}$ rad.

The response surface for the control effort index CE is shown in Figure 59. As one can see measurement errors have no significant effect on the control effort. Hence, the system cannot fail because of excessive torque requirements due to measurement errors. Changes in the load torque do however affect the control effort index CE. If the load torque is much higher than expected, then the motor will go into saturation or even be destroyed. By looking at the phase currents we can however ensure that this is not the case for the

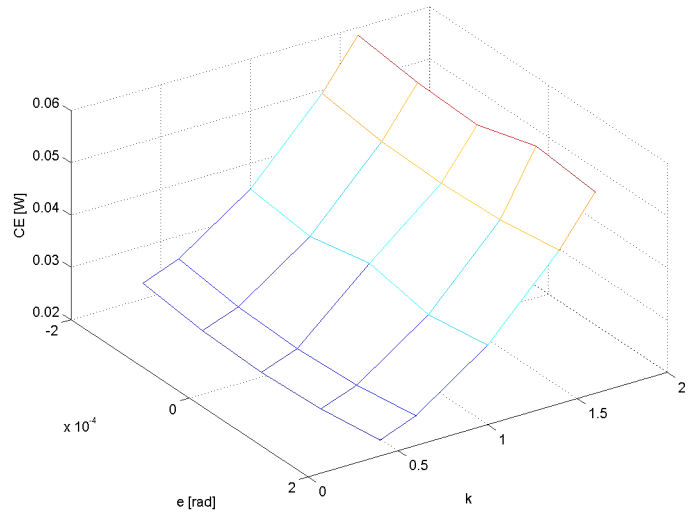

Figure 59: CE response surface for changes in plant parameters.

range of plant parameters shown in Figure 59. As a result control effort is also robust for the given change of parameters.

The criteria for empirical validity described in Section 8.3 have therefore been fulfilled. We conclude that the system has empirical performance validity.

8.5 Theoretical Performance Validity

We now come to the last quadrant of the Validation Square. We intend to demonstrate that the system has validity going beyond the previously discussed examples. Hence, we want to show that the model and controller can be modified and applied to a broader field. We believe that this can be done due to the following characteristics.

- Modularity: Both the model and the controller have been based on the concept of modularity. We have made effective use of modularity by modifying the controller and the plant at multiple instances. This can be carried further if needed. Parts of the plant or controller can be easily modified without affecting others. Then the analysis tools developed in this chapter can be applied. We illustrate this concept by replacing the estimator with a sensor for $\dot{\delta}_{sup}$. Due to modularity the resulting changes in the controller can be implemented rapidly. We implemented it and show the resulting

responses for CP and variations in T in Figure 60. Using this figure it is now possible

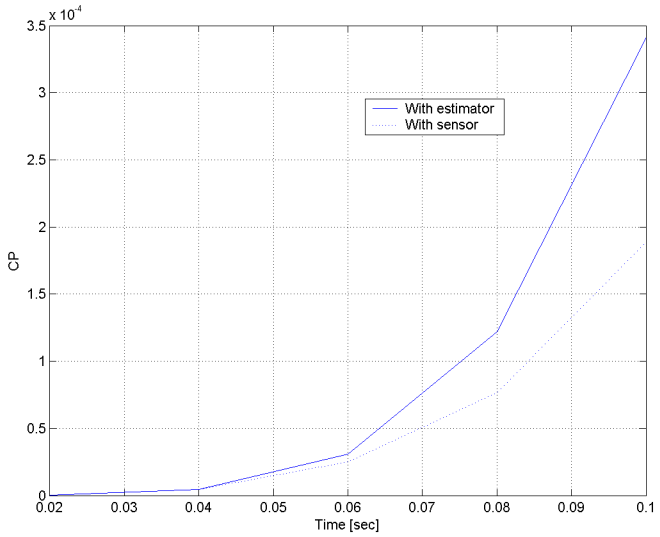

Figure 60: Comparison of CP for estimator and sensor.

to quantify the benefit of a sensor as compared to an estimator.

- Plant and controller parameterization: The plant and the controller have been developed in full generality without a specific vehicle in mind. It is only at the end of each modeling chapter that we introduced vehicle parameters (see Tables 5, 6 and 9). The vehicle parameters have not been integrated into the Simulink model, but were stored as separate MATLAB data files. The actual Simulink implementation can be seen in Appendix A. The advantage of this approach is easy adaptability. If one wants to use the model for another type of vehicle, all one needs to do is change the parameters in the MATLAB data file. The same is true of the controller. Control parameters have not been expressed numerically, but in terms of performance parameters such as the natural frequency ω_0 or the sampling period T. Hence, the performance of the controller can be adapted easily by changing these parameters.

Based on the above examples we conclude that the given design is sufficiently open to accomodate a broad range of changes in terms of plant characteristics and desired performance. The effect of design changes can be measured using the performance indices and analysis

tools used in this chapter. By obtaining more information on the cost of individual components, one could also introduce cost as a quantifiable design criterion. If we want to take our design even closer to its actual implementation in the vehicle, then this should be the path to be followed.

APPENDIX A

SIMULINK IMPLEMENTATION

The Simulink model has been structured in exactly the same manner as the model and the controller described in the previous chapters (Figure 61). On the highest level are the three

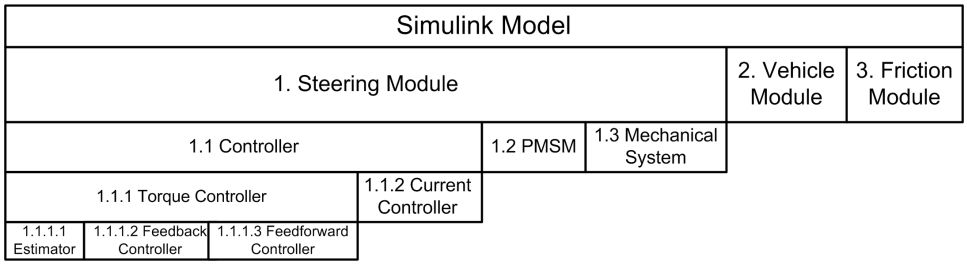

Figure 61: Structure of Simulink implementation.

modules, i.e., steering module, vehicle module and friction module. Moreover, there are the submodules of the steering module, namely the controller, the PMSM and the mechanical system. The controller has been divided into the torque and the current controller. Finally, the torque controller comprises the estimator, the feedback and the feedforward controller. In the following sections we give screenshots of all Simulink modules.

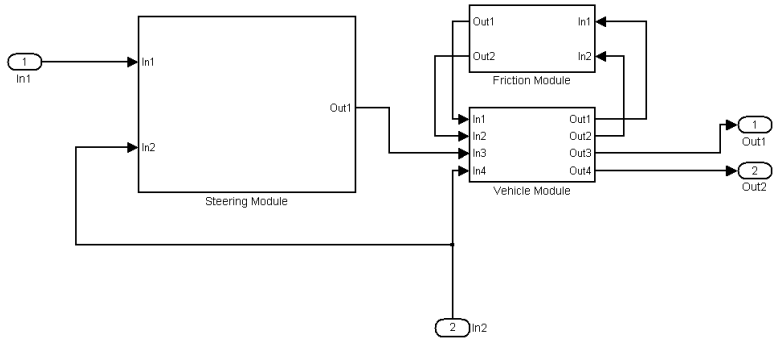

Figure 62: Simulation model.

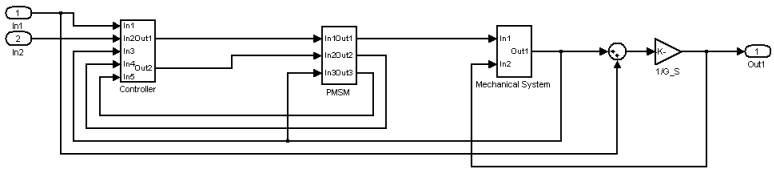

Figure 63: Steering module.

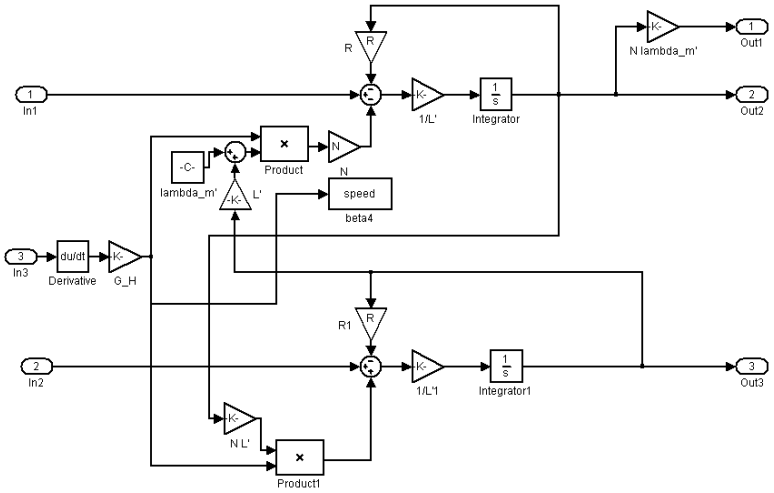

Figure 64: PMSM.

A.1 Steering Module

A.1.1 Controller

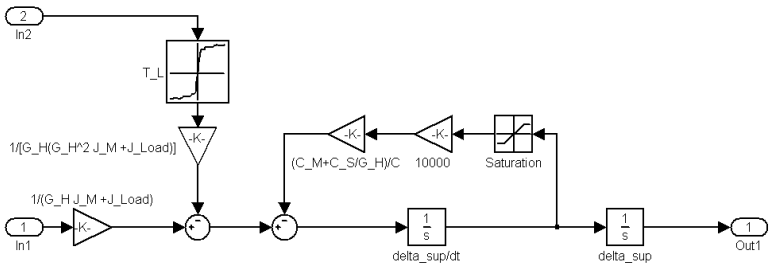

Figure 65: Mechanical System.

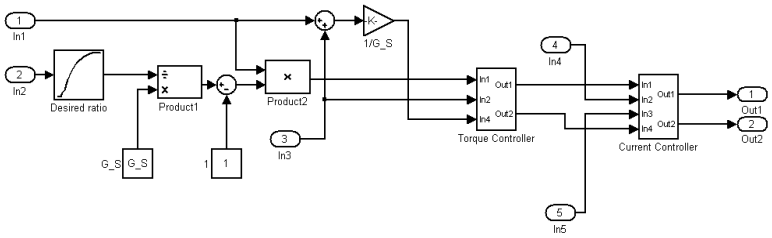

Figure 66: Controller.

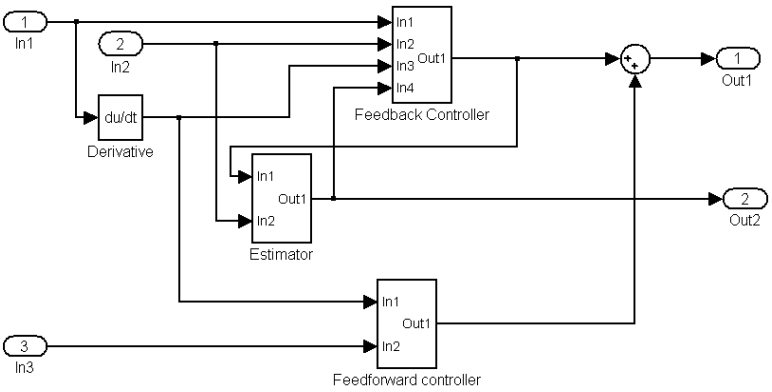

Figure 67: Torque controller.

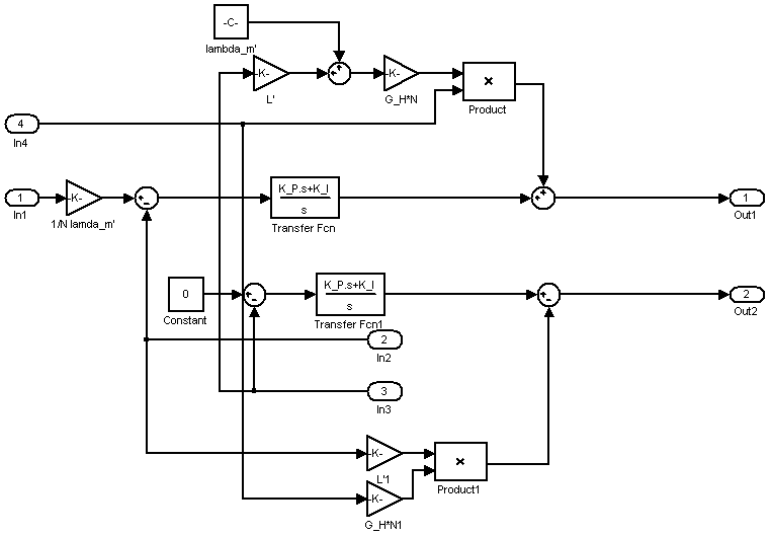

Figure 68: Current controller.

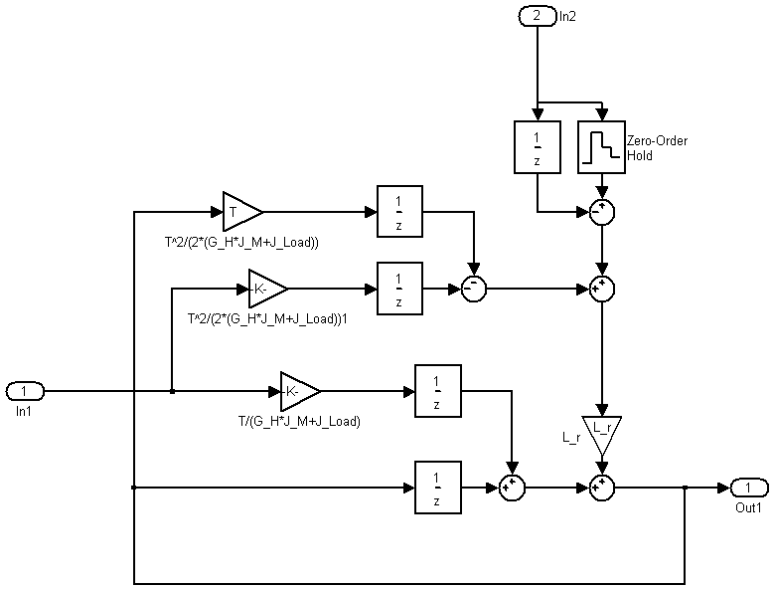

Figure 69: Estimator.

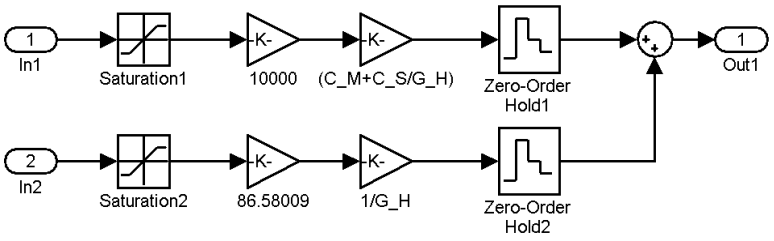

Figure 70: Feedback controller.

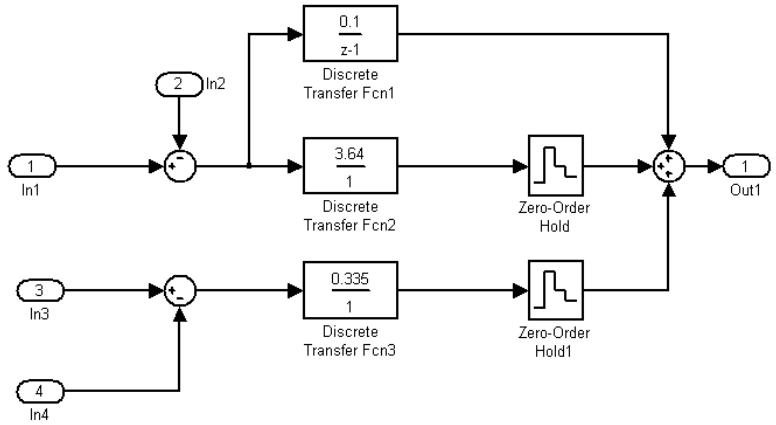

Figure 71: Feedforward controller.

A.2 Vehicle Module

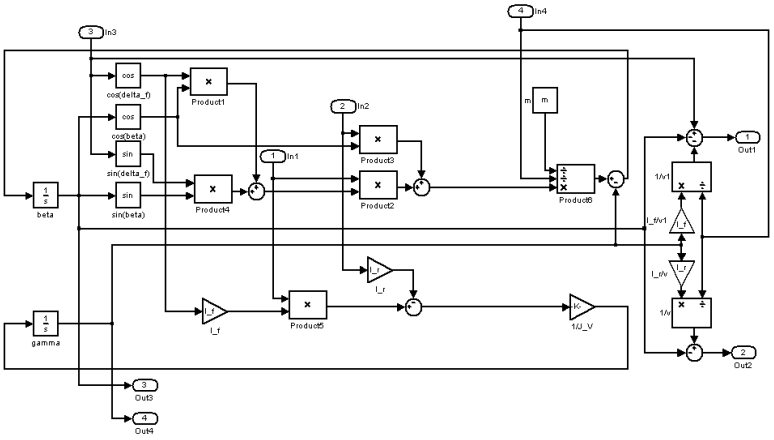

Figure 72: Vehicle module.

A.3 Friction Module

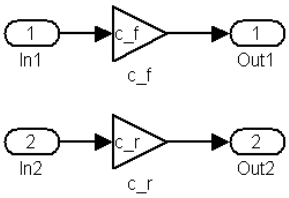

Figure 73: Friction module.

REFERENCES

[1] Bakker, E. and Pacejka, H., "Magic formula tyre model," *Vehicle System Dynamics*, vol. 21, pp. 1–18, 1993.

[2] Chen, C.-T., *Analog and Digital Control System Design: Transfer-Function, State-Space, and Algebraic Methods*. Saunders College Publishing, 1993.

[3] Chen, W., Allen, J., Mavris, D., and Mistree, F., "Concept exploration method for determining robust top-level specifications," *Engineering Optimization*, vol. 26, no. 2, pp. 137–158, 1996.

[4] Crowder, R., *Electric Drives and Their Controls*. Oxford University Press, 1995.

[5] de Wit, C., Olsson, H., Astrom, K., and Lischinsky, P., "A new model for control of systems with friction," *IEEE Transactions on Automatic Control*, vol. 40, no. 3, pp. 419–425, 1995.

[6] DeMeis, R., "BMW opts for hybrid steering system," *Design News*, vol. 17, pp. 46–47, 2003.

[7] Franklin, G., Powell, J., and Workman, M., *Digital Control of Dynamic Systems*. Addison Wesley Publishing, 1992.

[8] Fukao, T., Miyasaka, S., Mori, K., Adachi, N., and Osuka, K., "Active steering systems based on model reference adaptive nonlinear control," 2001 IEEE Intelligent Transportation Systems Conference Proceedings, pp. 502–507.

[9] Grenier, D., Mende, R., and Louis, J., "Comparison of several control strategies for d.c. brushless drives," vol. 1 of *Proceedings of IECON'94 - 20th Annual Conference of IEEE Industrial Electronics*, pp. 26–31, 1994.

[10] Jahns, T., "Motion control with permanent-magnet ac machines," *Proceedings of the IEEE*, vol. 82, no. 8, pp. 1241–1452, 1994.

[11] Khalil, H., *Nonlinear Systems*. Prentice Hall, 2002.

[12] Khan, W. and Taylor, D., "Adaptive control of ac motor drives with inverter nonlinearities," *International Journal of Control*, vol. 72, no. 9, pp. 784–798, 1999.

[13] Krause, P., Wasynczuk, O., and Sudhoff, S., *Analysis of Electric Machinery and Drive Systems*. IEEE Press, 2002.

[14] Mammar, S. and Baghdassarian, V., "Two-degree-of-freedom formulation of vehicle handling improvement by active steering," vol. 1 of *Proceedings of the 2000 American Control Conference*, pp. 105–109, 2000.

[15] McCann, R., Pujara, L., and Lieh, J., "Influence of motor drive parameters on the robust stability of electric power steering systems," *Power Electronics in Transportation*, vol. 38, no. 3, pp. 103–108, 1998.

[16] Miller, T., *Brushless Permanent-Magnet and Reluctance Motor Drives*. Oxford University Press, 1989.

[17] Nagai, M., Shino, M., and Gao, F., "Study on integrated control of active front steer angle and direct yaw moment," vol. 23, no. 3, pp. 309–315, 2002.

[18] Ono, E., Hosoe, S., Doi, S., Asano, K., and Hayashi, Y., "Theoretical approach for improving the vehicle robust stability and manoeuvrability by active front wheel steering control," vol. 29, pp. 748–753, 1998.

[19] Pedersen, K., Emblemsvag, J., Bailey, R., Allen, J., and Mistree, F., "Validating design methods & research: The validation square," vol. 4 of *Proceedings of the 2000 ASME Design Theory and Methodology Conference*, 2000.

[20] Riekert, P. and Schunk, T., "Zur Fahrmechanik des gummibereiften Kraftfahrzeuges," vol. 11, pp. 210–224, 1940.

[21] Shames, I., *Engineering Mechanics: Dynamics*. Prenctice Hall, 1960.

[22] Tagawa, Y., Ogata, H., Morita, K., Nagai, M., and Mori, H., "Robust active steering system taking account of nonlinear dynamics," vol. 25 of *Vehicle System Dynamics*, pp. 668–681, 1996.